Explorer la physique aux interfaces d'oxydes fortement corrélées: résultats récents et perspectives en microscopie électronique.

Alexandre Gloter et Odile Stephan (LPS, Université Paris-Sud, 91405 Orsay)

1. STEM imaging & EELS principles

1.1 A few generalities about transmission microscopy

1.2 Image formation principles in STEM and examples

1.3 EELS principles and examples

2. Application to oxide thin films

2.1. Strain relaxation in LAO/STO bilayers

2.2. Oxygen octahedra rotation in LSMO

2.3. Textured VO2 thin film on sapphire

3. Few perspectives on STEM-EELS for oxides / interfaces studies

Transmission Microscopy

Microscope = Source + Lenses + detector

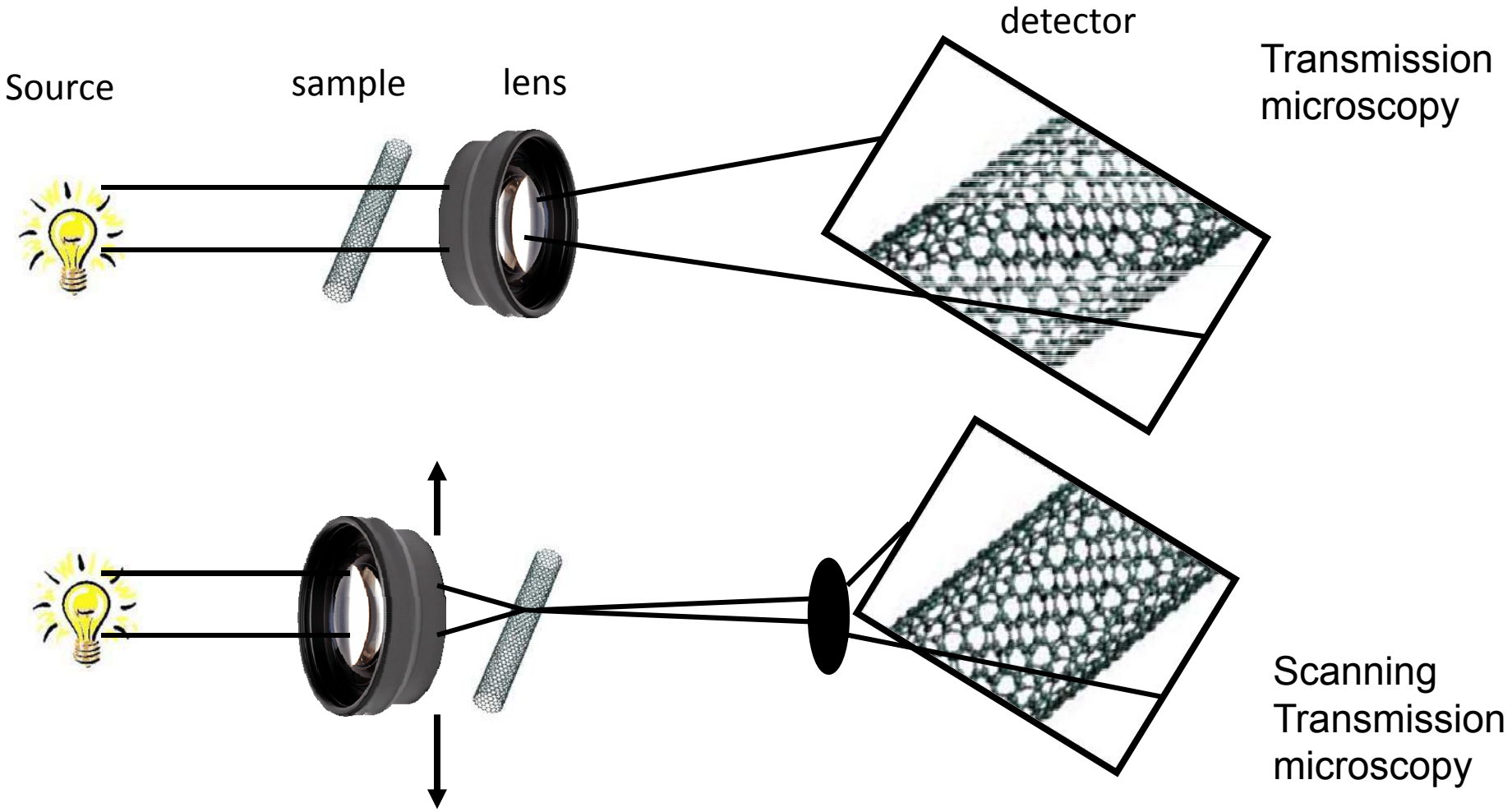

Overcoming diffraction the limit in optical transmission optical / X-ray microscopy

Optical microscope
Wavelength ca. 400-700 nm

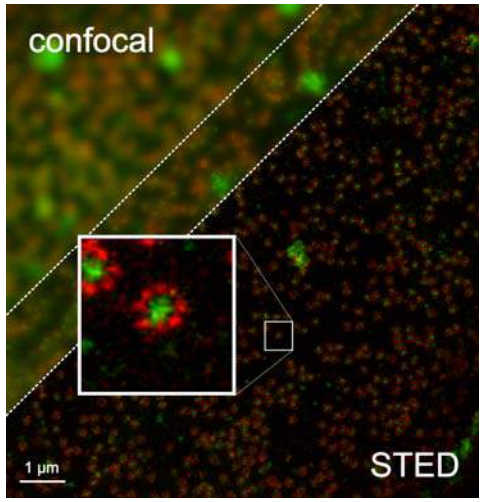

Nobel Prize in
Chemistry 2014

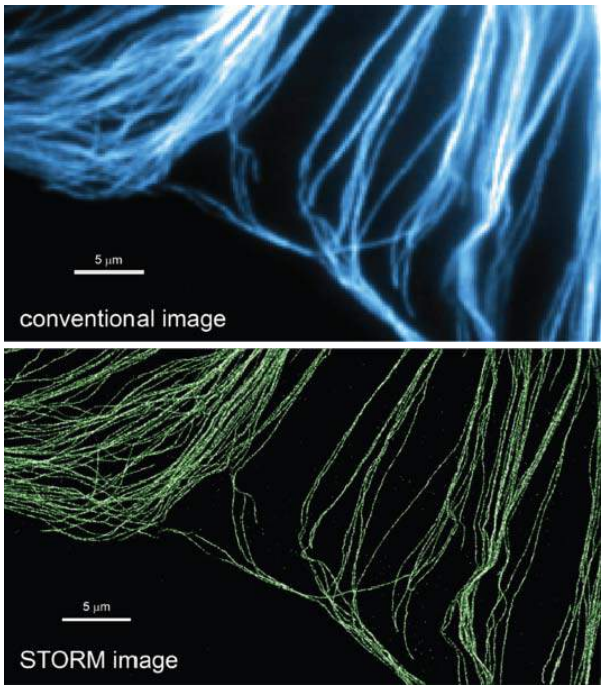

Images of microtubules in a cell. Microtubules are immunolabeled with photoswitchable dyes.

Conventional fluorescence images (resolution 500 nm)

STORM images
http://zhuang.harvard.edu/storm.html

X-ray microscope
Wavelength ca. 1-5 nm

STXM image of latex sphere
Resolution around 50nm

From
http://sls.web.psi.ch/view.php/beamlines/pollux/status.html

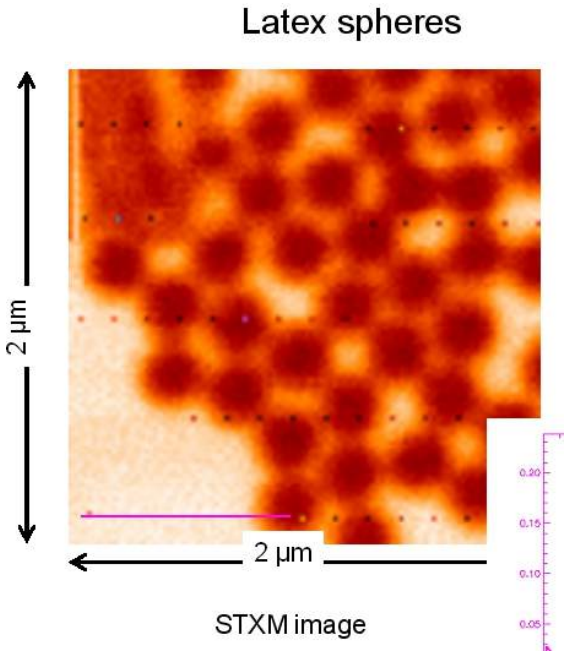

Why use electrons ?

Electrons are charged particles:
their trajectories can be efficiently changed with E.M. lenses

Electrons are waves:

- wave optics should apply to image formation principles
- their wavelenght can be reduced much below 1 Å when accelerated

100 keV = 3 pm.

The (diffraction limited) resolution
in TEM should be a few pm

Resolution and spatial frequency (the transfer function of the instrument)

$SrTiO_3$ model image (Z contrast)

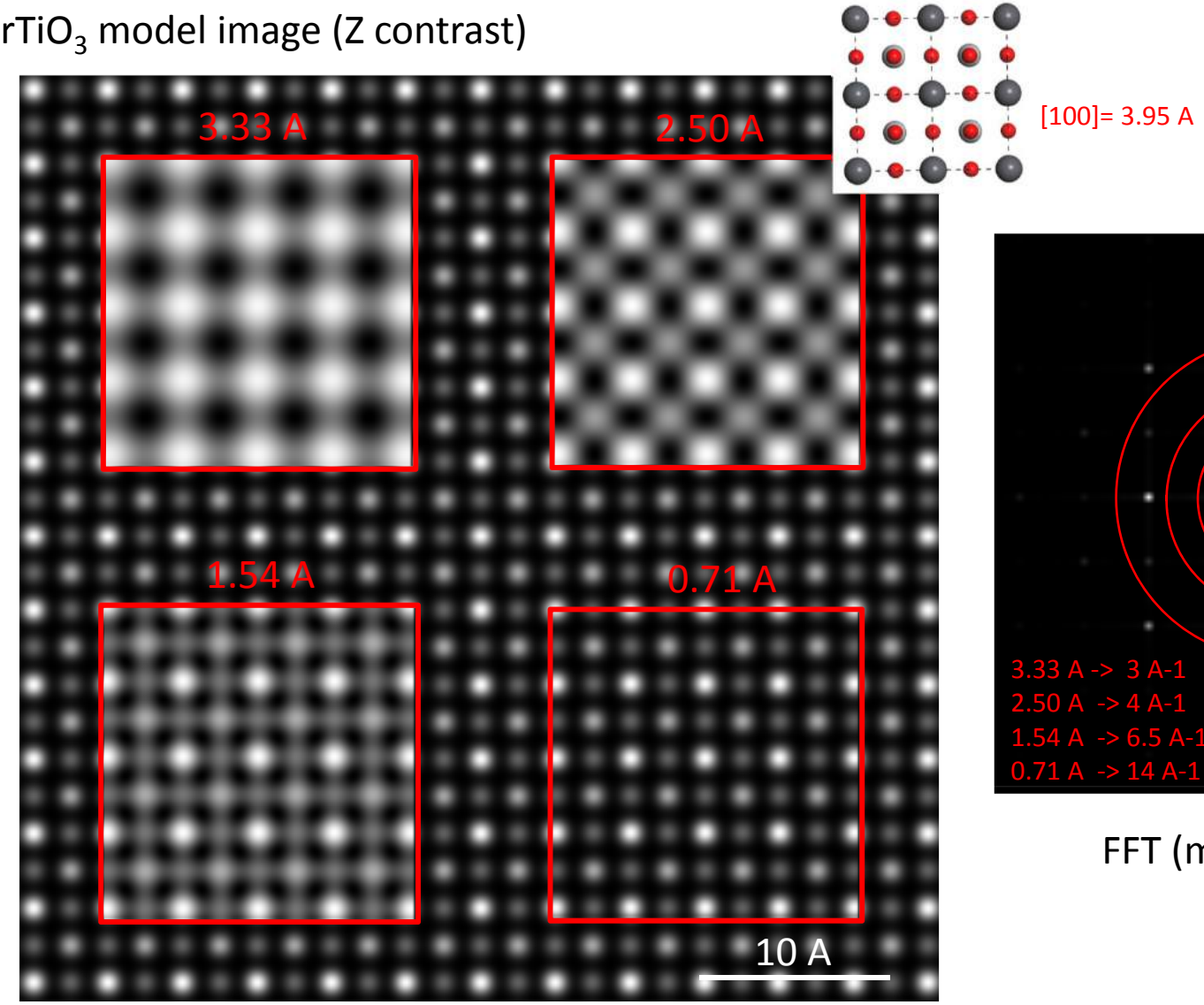

[100]= 3.95 A

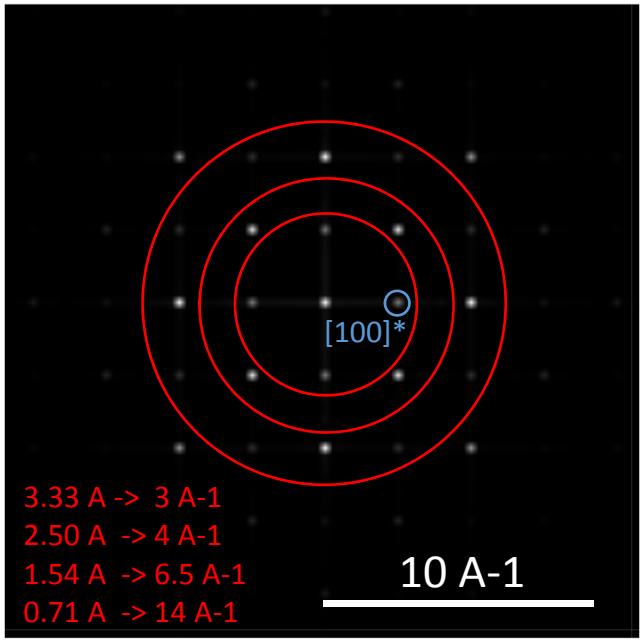

FFT (module) and filter

In practice, an electron microscope is a set of E.M. lenses and multipoles

a

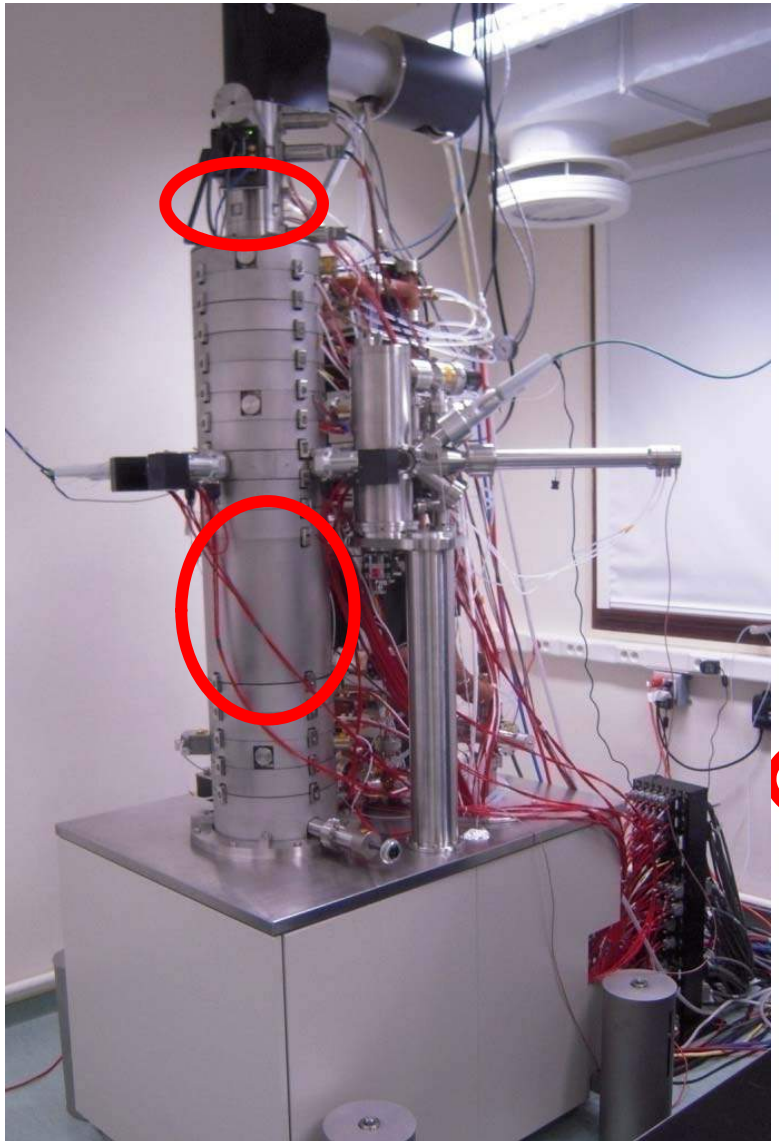

b

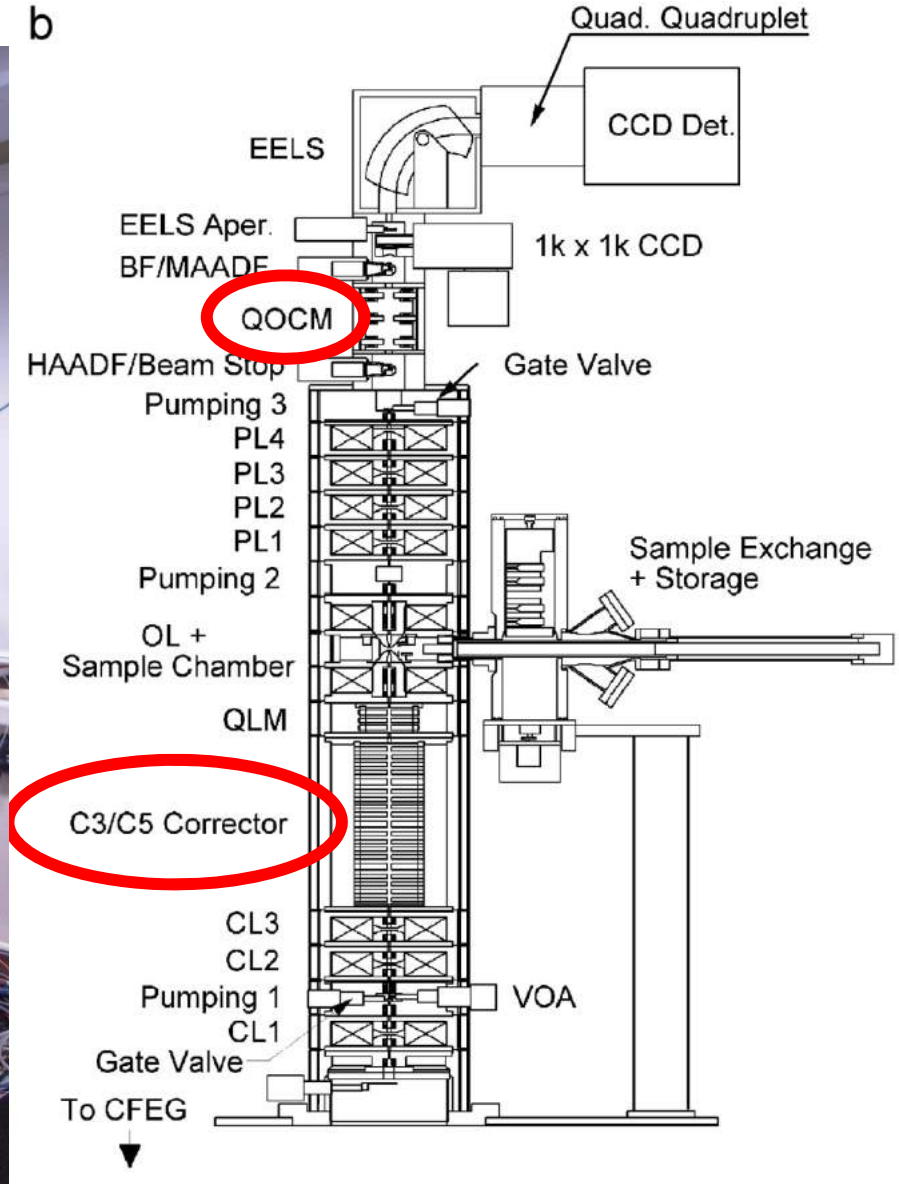

Nion 60-100 keV prototype 1 (CNRS-Orsay), CFEG, UHV columns
Resolution 0.1 nm (100keV) Energy resolution < 0.4 eV

An optical system is diffraction limited

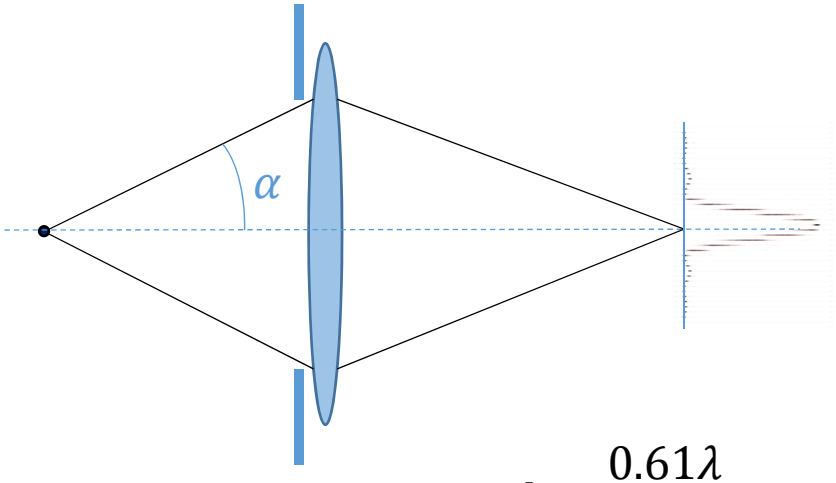

$$d = \frac{0.61\lambda}{\eta \sin \alpha}$$

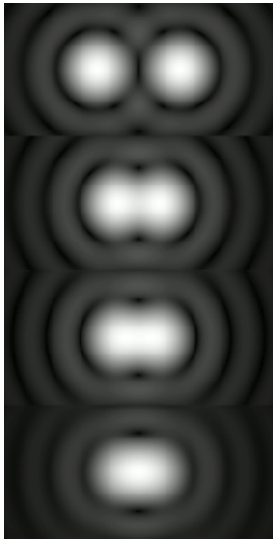

Rayleigh criterion

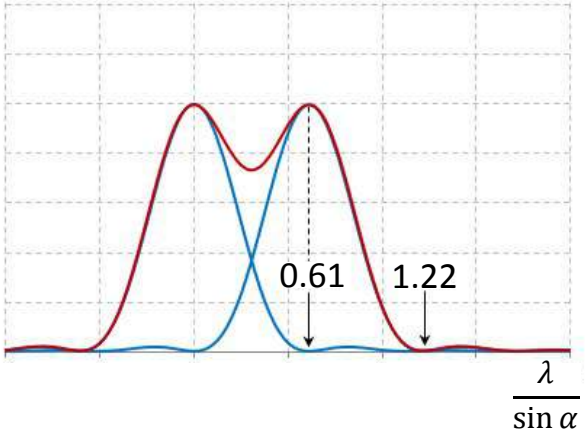

Light microscope

$\lambda \sim 0.5\ \mu m$

$\eta = 1.5\ (glass)$

$\alpha \sim 70°$

$d \sim 0.21\ \mu m$

Electron microscope

$\lambda \sim \frac{h}{\sqrt{2m_0 eV_0}} = 3.4\ pm$ (100 keV)

$\eta = 1\ (vacuum)$

$for\ \alpha \sim 30°$

$d \sim 3.4\ pm$!!!!!

In practice

$\alpha \sim 1 - 3\ .\ 10\ mrad$

Because lenses have…

Aberrations……..

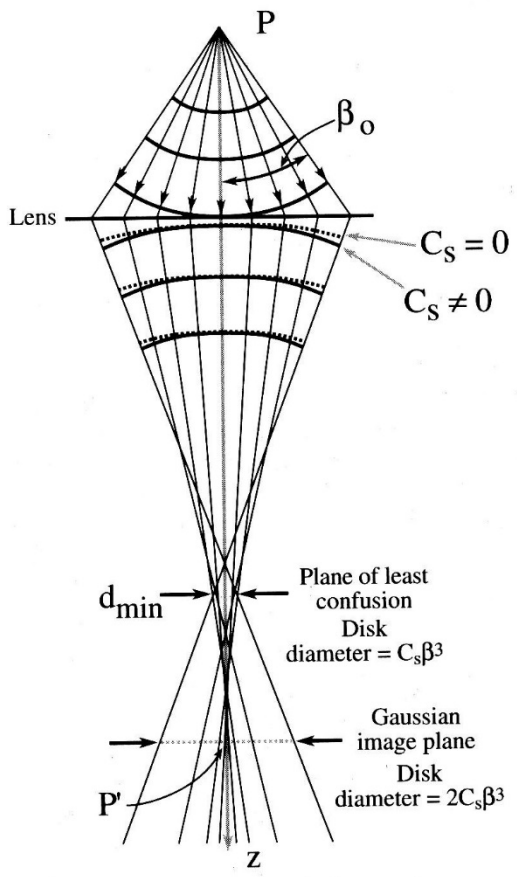

Figure 6.11. Spherical aberration in the lens causes wavefronts from a point object P to be spherically distorted. The point is thus imaged as a disk with a minimum radius in the plane of least confusion and a larger disc at P' in the Gaussian image plane.

From D.B Carter and C.B. Barry

- **Spherical aberration**

SA disk, $r_{sph} = C_s\beta^3$

- **Chromatic aberration**

CA disk, $r_{chr} = C_c(\Delta E/E_0)\beta$

- **Resolution**

Cs = 1.1 mm; Cc = 1.5 mm

E_0 = 300 keV (deBroglie wavelength 2.51 pm), ΔE = 1eV

HREM point to point resolution is around 0.2 nm

Optimized convergence angle

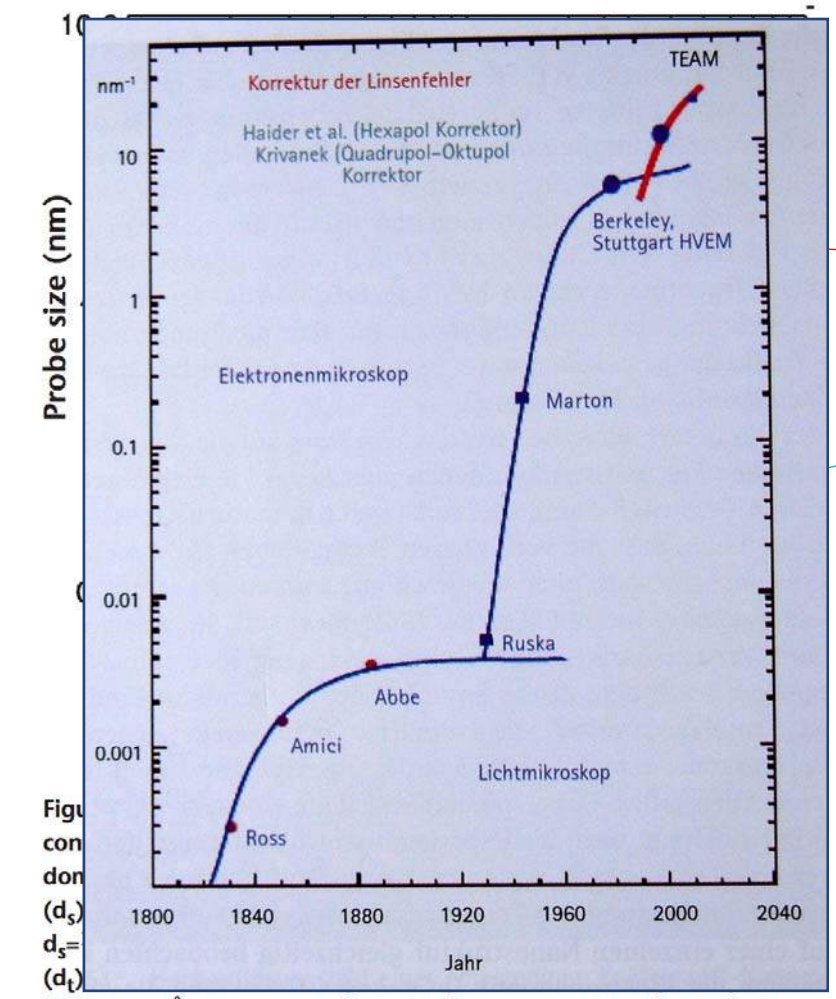

size of ~2.8Å, which is a more pessimistic estimate than the wave optical treatment.

d_S=0.5 $C_s\alpha^3$

d_S=0.61 $\frac{\lambda}{\alpha}$

+ other effects:

- higher order geometrical aberrations
- chromatic aberrations
- extended source size
- instabilities

From M.Weyland and D.A. Muller (Cornell University)

Cs corrected microscopy

The correction of the round lens spherical abberation (Cs > 0) is obtained by a combination of lower symetry electron optic elements such as quadrupole, hexapole, octupole (whose Cs can be made < 0 along some directions)

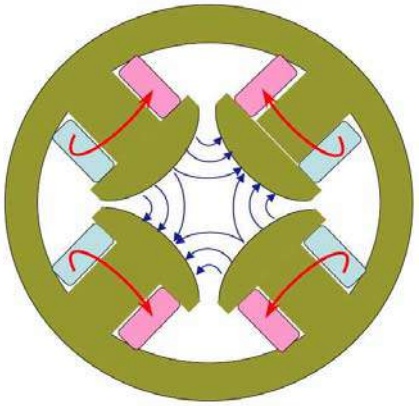

If the quadrupole poles are of the perfect shape (hyperbolic), it generates constant magnetic field gradient *B'*, which acts as a focusing lens in *x* and defocusing in *y*, or vice versa

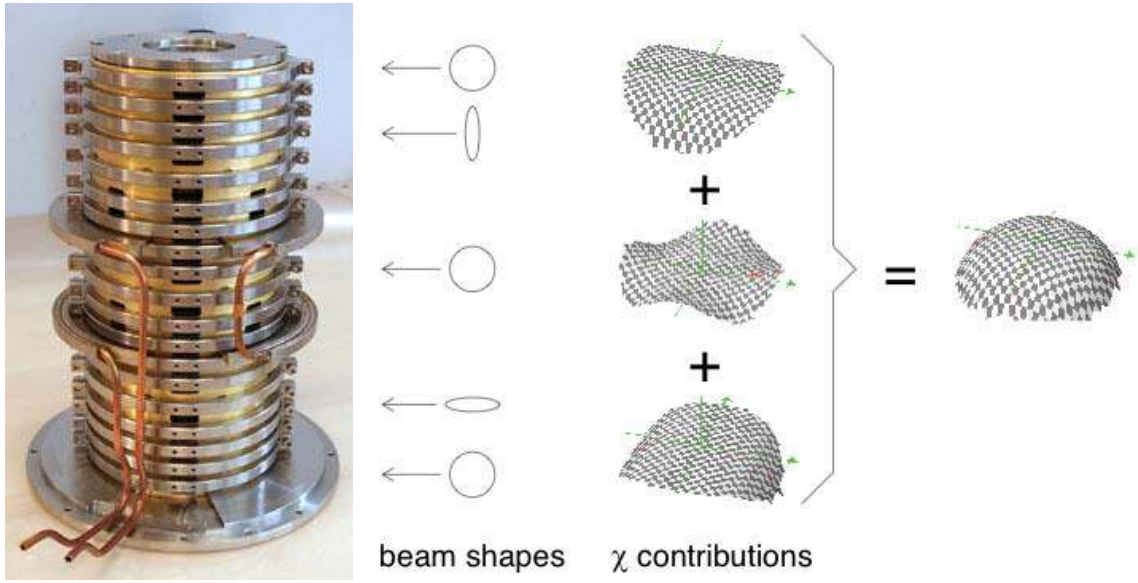

Krivanek et al. Ultramicroscopy 108 (2008) 179–195.
www.nion.com

Image formation principles in STEM

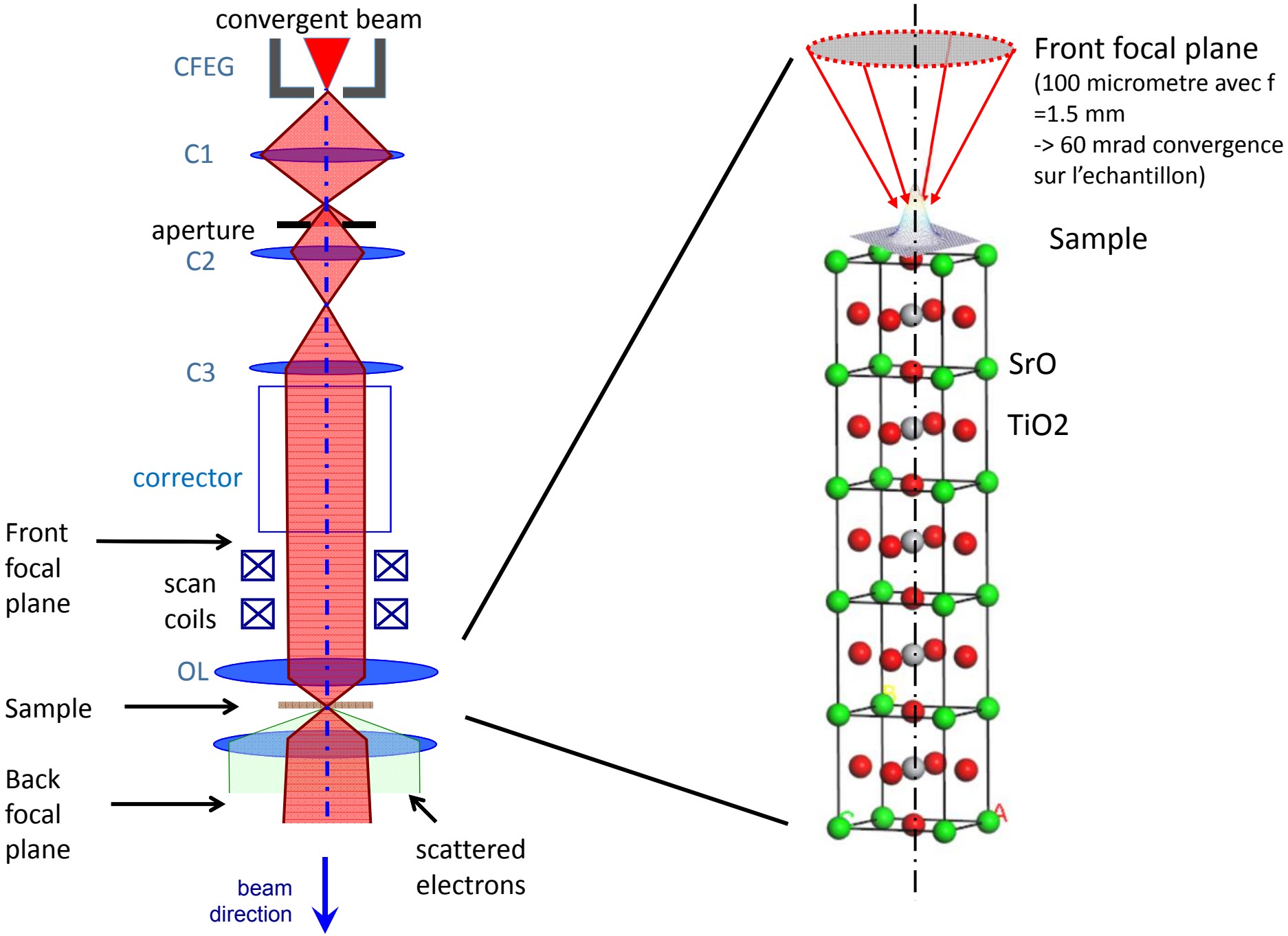

Wave function propagation along a Ti-O Column

Wave function (modulus)

Diffraction

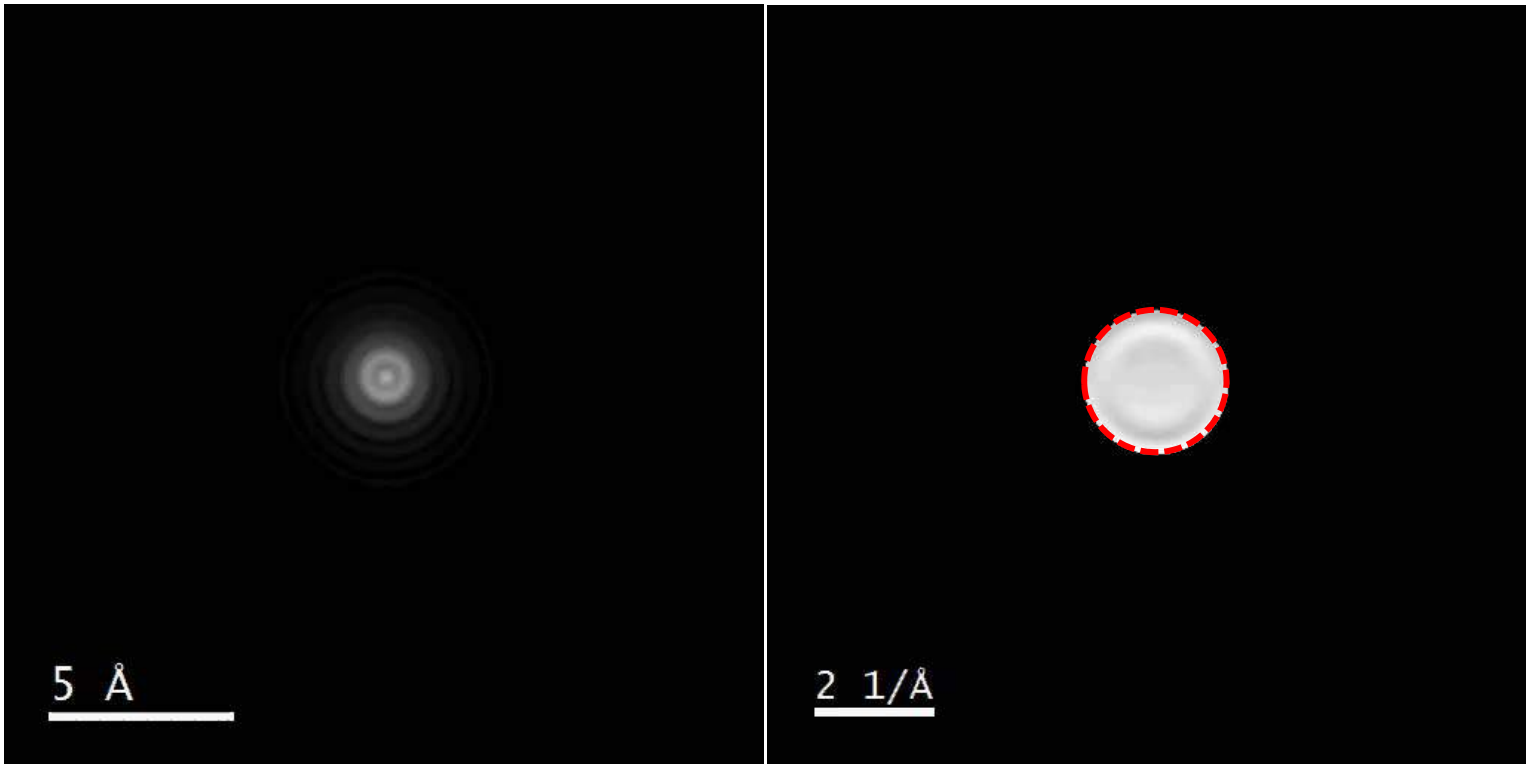

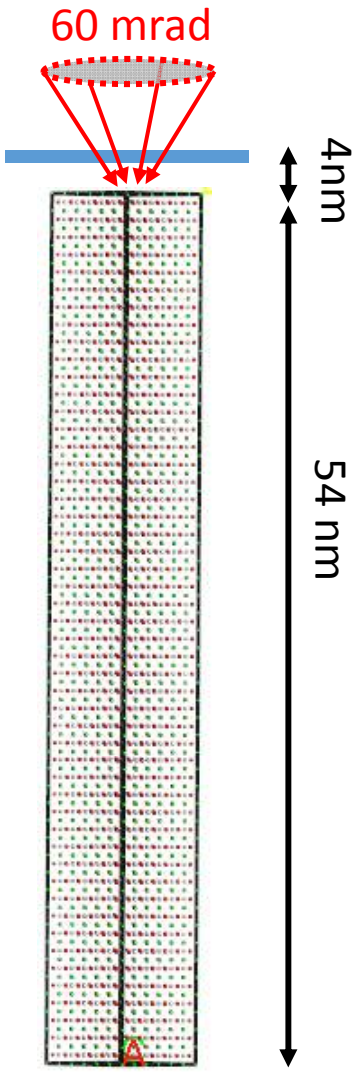

Image formation in a STEM/ geometry of the detectors

Incident wave function $\Psi_p(\vec{x}, \vec{x}_p)$

Exit wave function $\Psi_t(\vec{x}, \vec{x}_p) = \Psi_p(\vec{x} - \vec{x}_p).t(\vec{x})$

Specimen transmission function $t(\vec{x}) \sim e^{i\sigma V_z(\vec{x})}$

Wave function in the diffraction plane (CBED pattern) $\widetilde{\Psi}_t(\vec{q}, \vec{x}_p)$

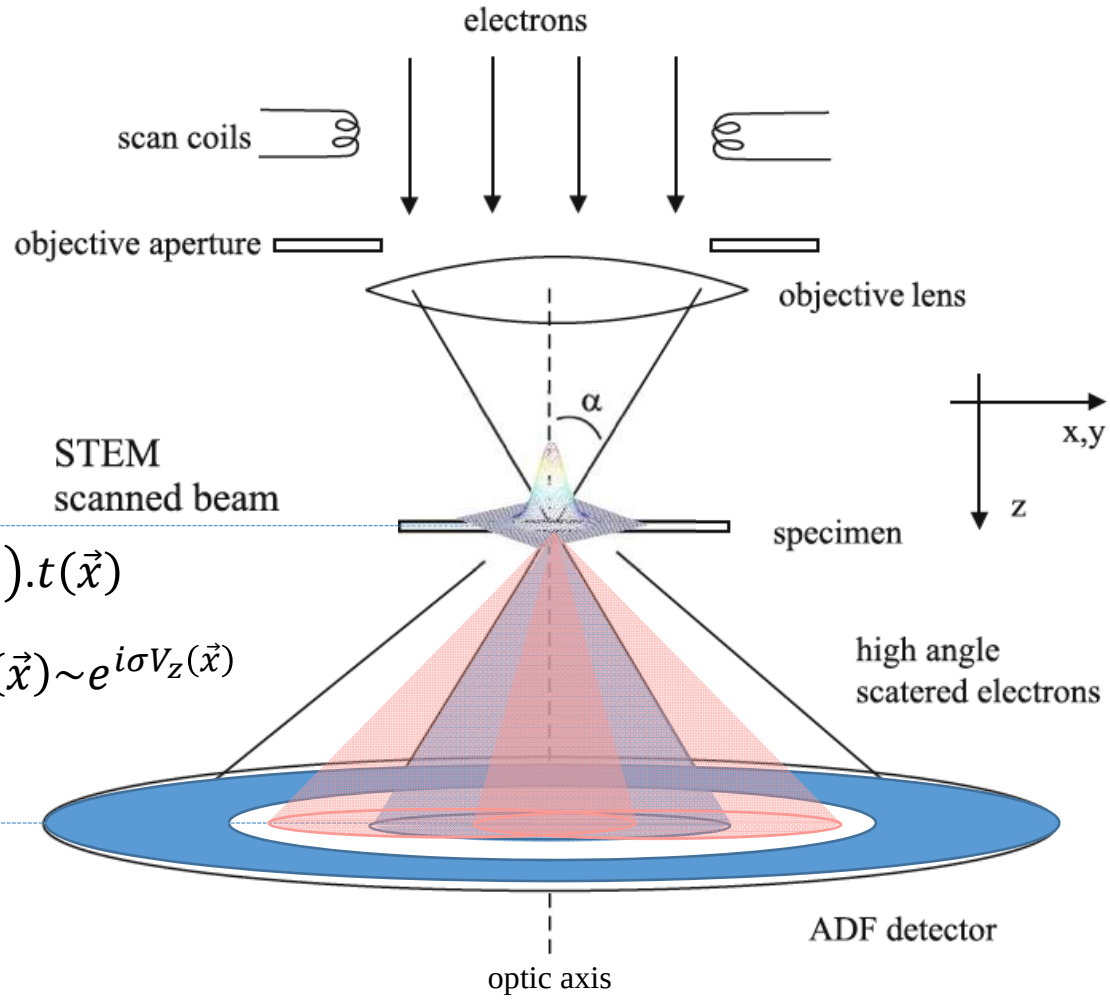

Simplified model of a STEM (the condenser and projector lenses are ignored)

Selecting the geometry of the detector to tune the nature of the contrast in the image

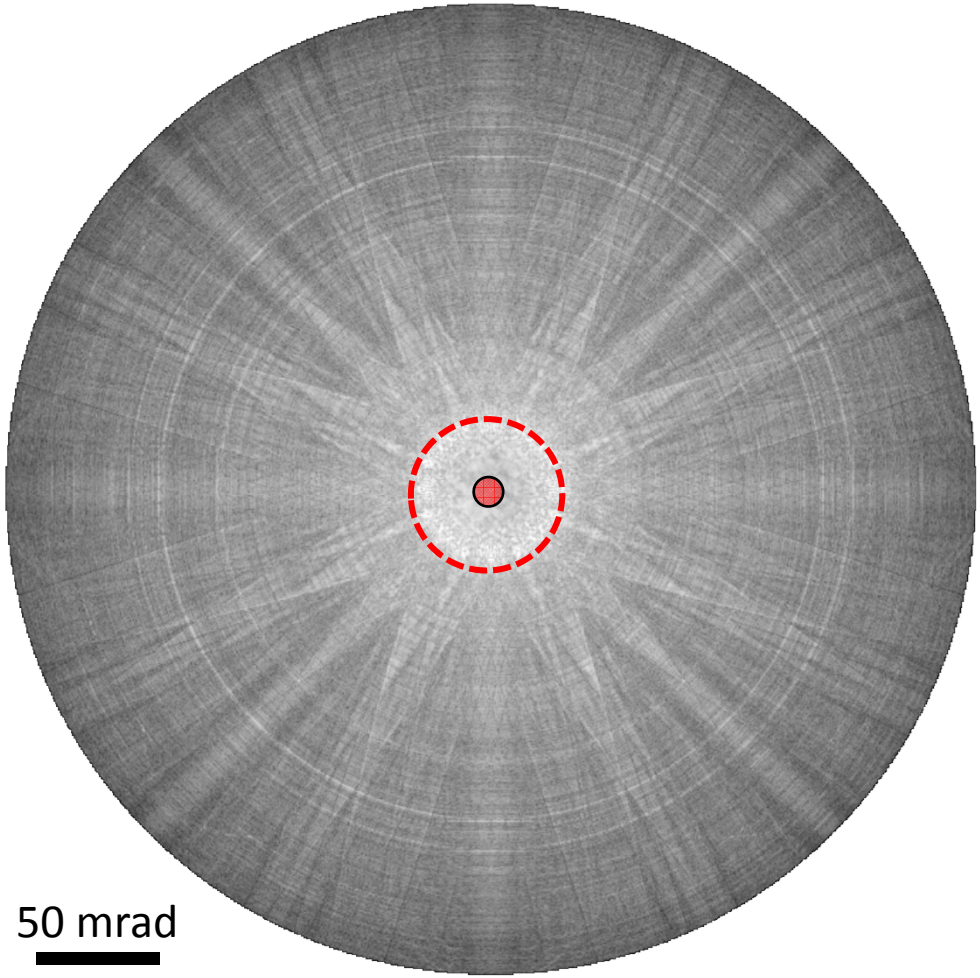

Diffraction pattern (CBED, log scale)
1 Å electron probe on a single Ti atomic column

Intensity in the image for one probe position $\overrightarrow{x_p}$: incoherent integration of the diffraction pattern over the geometry of the detector:

$$I(\vec{x}_p) = \int_{q_{Dmin}}^{q_{Dmax}} \left|\widetilde{\Psi}_t(\vec{q},\vec{x}_p)\right|^2 D(\vec{q}) d\vec{q}$$

$D(\vec{q})$ = 1 for $q_{Dmin} < q < q_{Dmin}$
= 0 otherwise

Coherent contrast (Bright Field image):

$$D(\vec{q}) \sim \delta(\vec{q})$$

$$I_{axial}^{BF}(\vec{x}_p) = \left|\widetilde{\Psi}_t(0,\vec{x}_p)\right|^2$$
$$= \left|\Psi_p(\vec{x}_p) * t(\vec{x}_p)\right|^2$$

Selecting the geometry of the detector to tune the nature of the contrast in the image

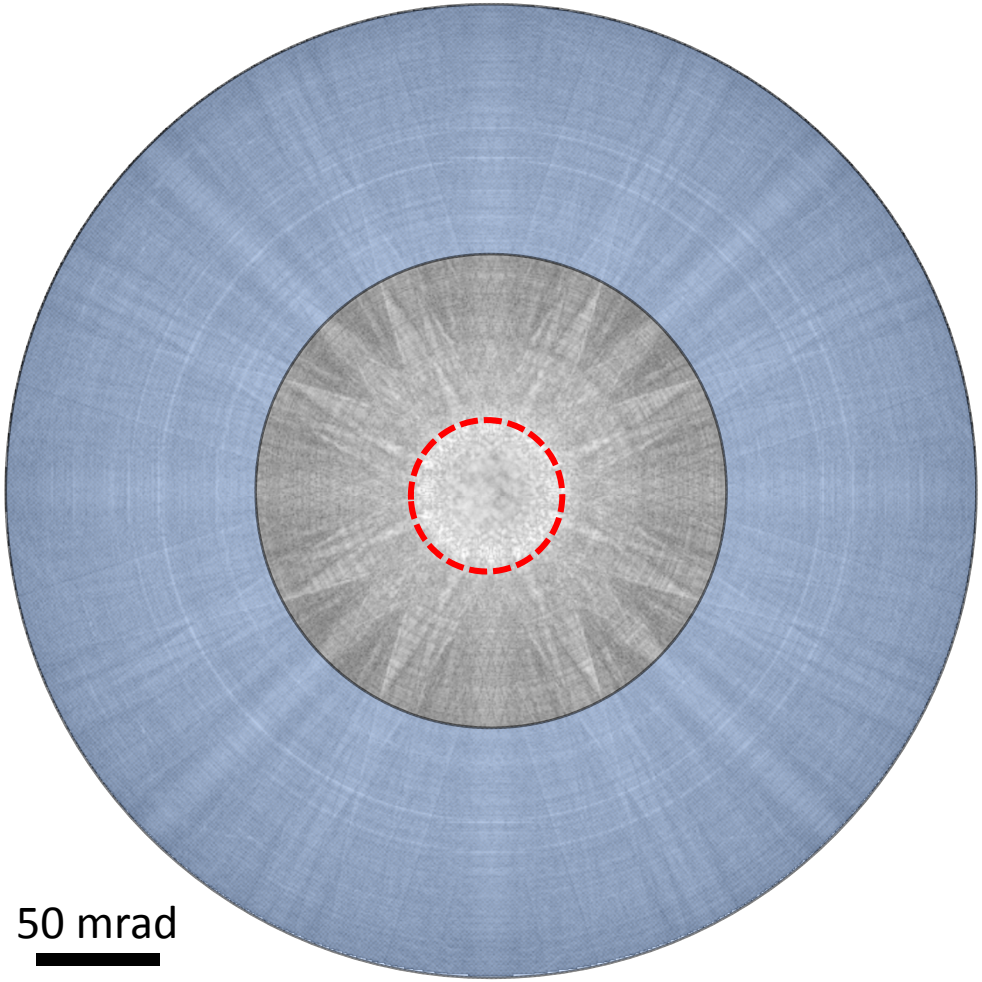

Diffraction pattern (CBED, log scale)
1 Å electron probe on a single Ti atomic column

Intensity in the image for one probe position $\overrightarrow{x_p}$: incoherent integration of the diffraction pattern over the geometry of the detector:

$$I(\vec{x}_p) = \int_{q_{Dmin}}^{q_{Dmax}} \left|\tilde{\Psi}_t(\vec{q}, \vec{x}_p)\right|^2 D(\vec{q}) d\vec{q}$$

$D(\vec{q})$ = 1 for $q_{Dmin} < q < q_{Dmin}$
= 0 otherwise

Incoherent contrast (High Angle Annular Dark Field image)

$$D(\vec{q}) = 1 - H(\vec{q})$$

$$I^{HAADF}(\vec{x}_p) = \left|\Psi_p(\vec{x}_p)\right|^2 * \left|A(\vec{x}_p)\right|^2$$

$$|A(\vec{x})|^2 \sim \int_{q_{Dmin}}^{q_{Dmax}} \frac{\partial \sigma(\vec{x})}{\partial q} d\vec{q}$$

Square of scattering factor at large angles $\sim Z^{1,5} - Z^{1,7}$

Detector geometry/image contrast/information

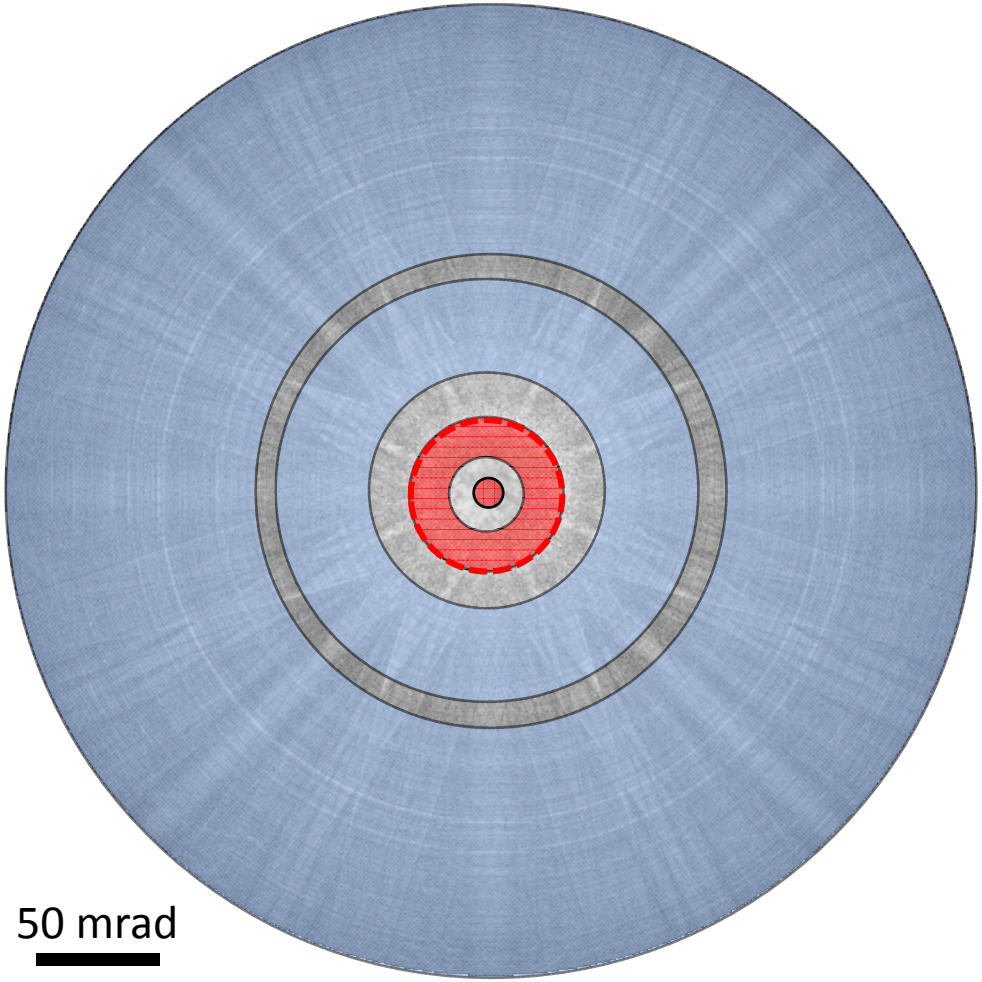

Diffraction pattern (CBED, log scale)
1 Å electron probe on a single Ti atomic column

BF : « true » phase contrast. Very sensitive to structural defects, weakly interpretable (phase)

ABF : phase contrast. Phase weakly modified by the sample. Light element imaging. Needs for a perfect correction of the lens aberrations (abberation (abberation = additional parasitic dephasing)

MAADF : semi-coherent contrast. Sensitive to strain and disorder

HAADF : « true » incoherent constrast.
Heavy element imaging. Precision of a few picometres (atomic displacements).

Quantitative BF / ABF

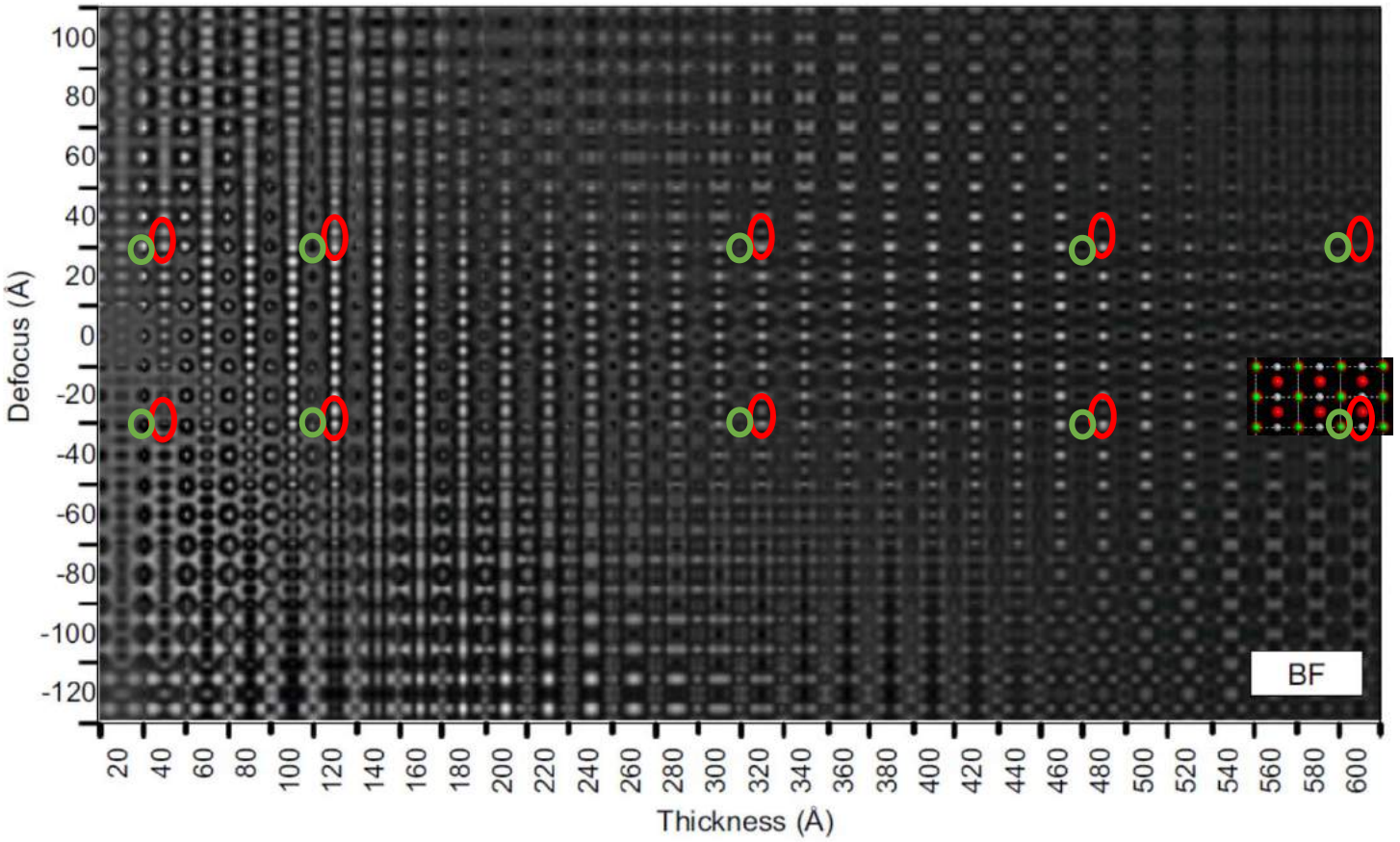

[110] SrTiO3

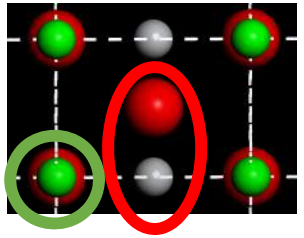

SrO TiO2

Quantitative BF / ABF

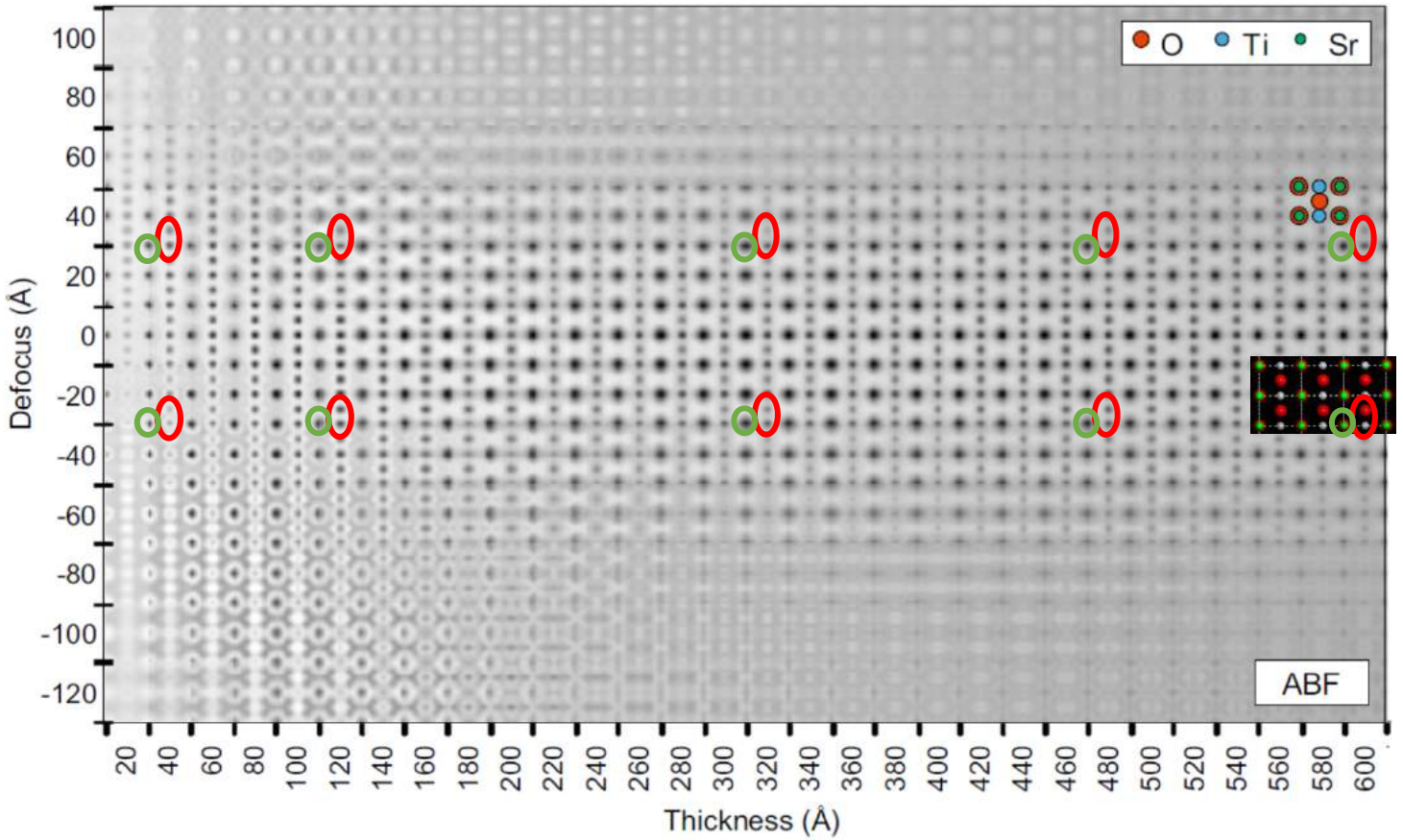

[110] SrTiO3

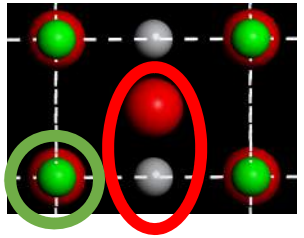

SrO TiO2

HAADF imaging (Z sensitive) superlattices and dopants

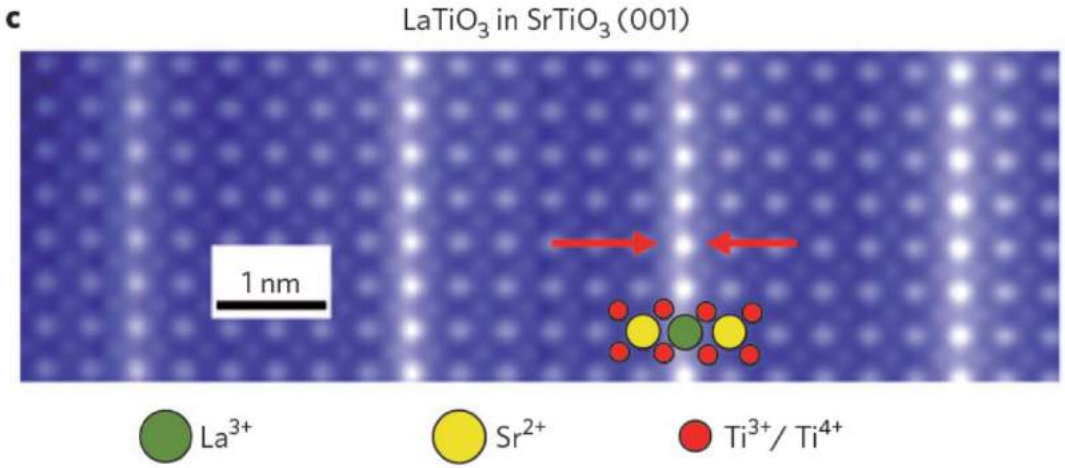

Single LTO layer for 5 STO
Hwang et al. Nat. Mat. 11 (2012)

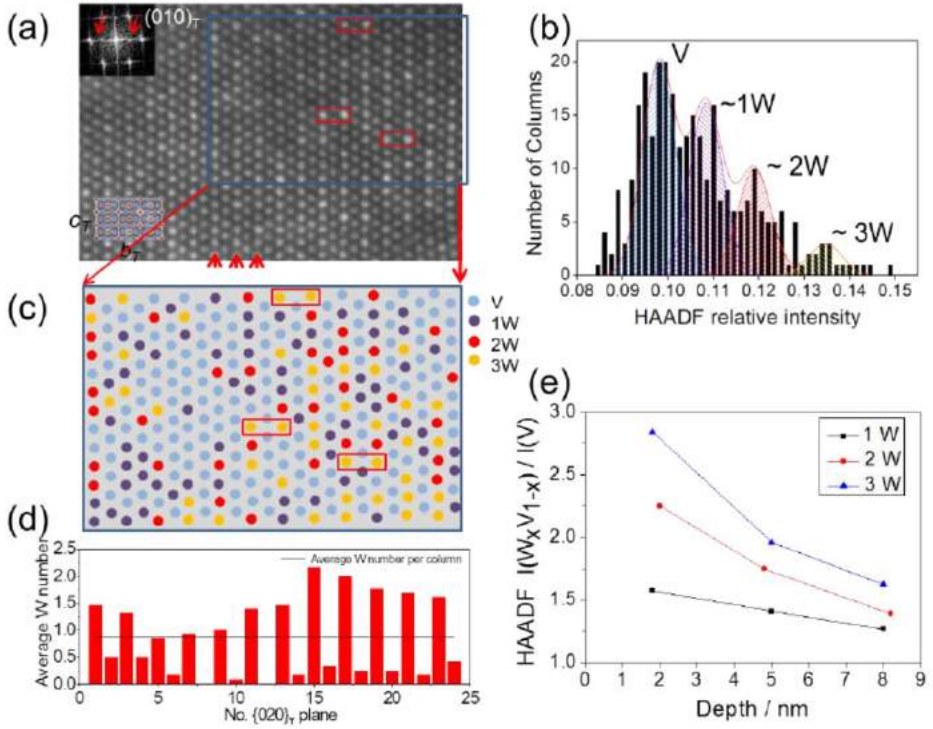

W doped VO_2
Li et al. Acta Materialia 80, (2014)

Observation of Vortex-antivortex structures in $PbTiO_3$ by STEM-HAADF imaging (pm displacements)

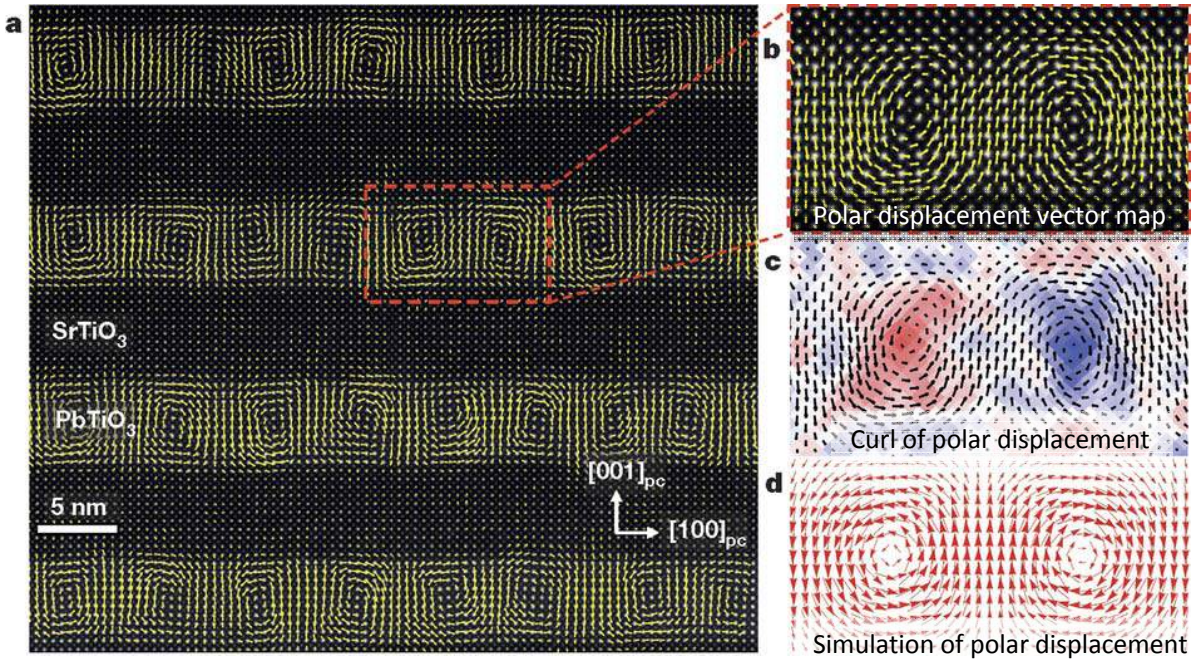

$(SrTiO_3)_{10}/(PbTiO_3)_{10}$ superlattice

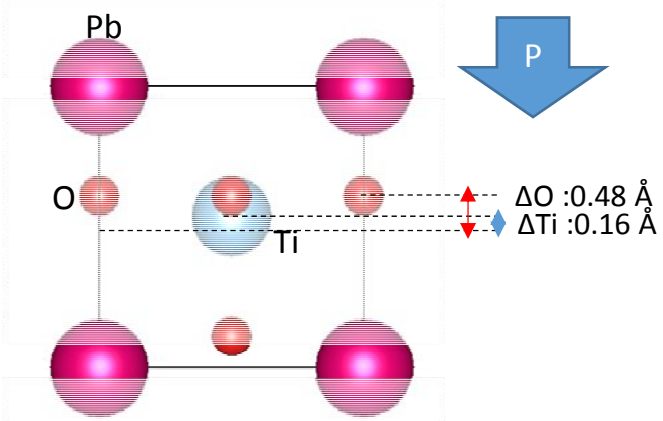

Complex topologies of electrical polarization

- For a range of superlattice periods, such vortex array can counterbalance the electrostatic energy rise of polar discontinuities at the PTO/STO interface, epitaxial constraints and domain formation.
- Inspiration for future physic: macro-scale charge ordering, electrically controllable chirality, new states of matter (dipolar skyrmions, hedgehog states),

A.K.Yadav, at.al., Nature 530 (2016) 198–201

Observation of polarization in $BiFeO_3$ combining ABF and HAADF imaging

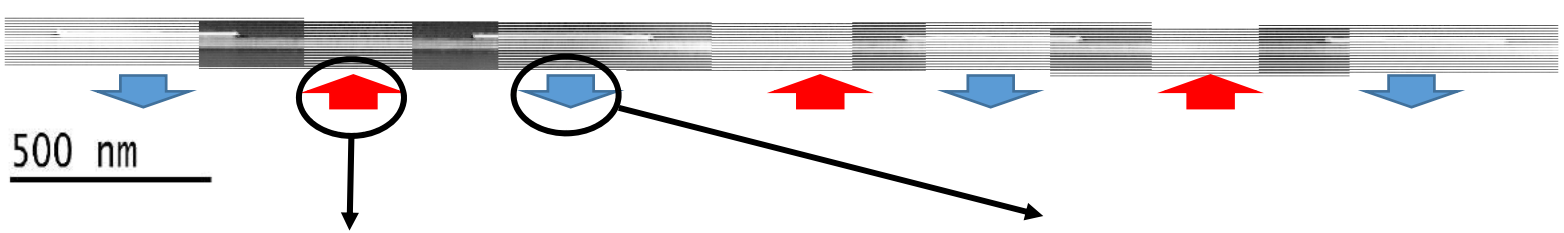

Electrode Pt/Co
$BiFeO_3$ (32nm) FE
$Ca_{0.96}Ce_{0.04}MnO_3$(20nm)
@ Substrate $YAlO_3$

HAADF ABF HAADF ABF

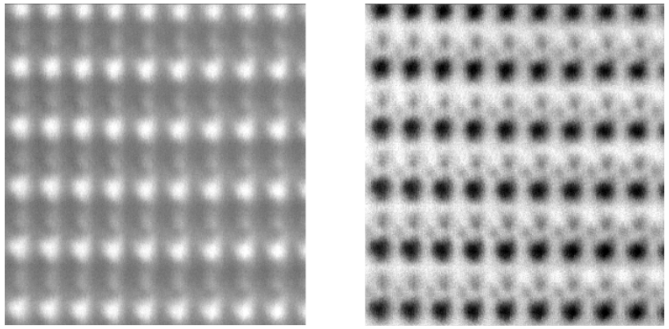

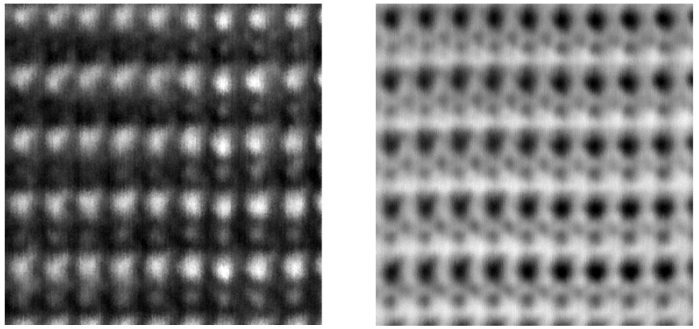

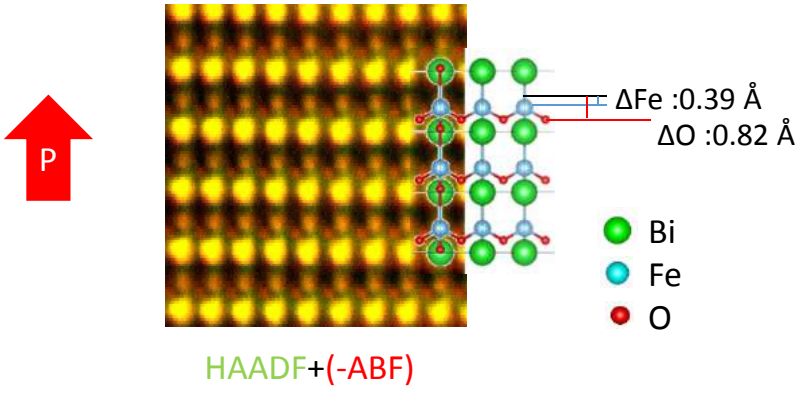

HAADF+(-ABF)

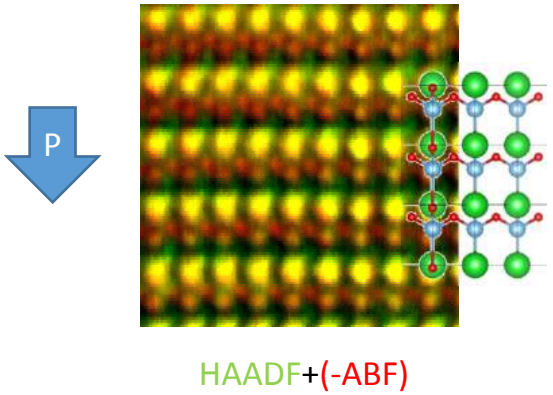

HAADF+(-ABF)

Coll. V. Garcia, S. Fusil, M. Bibes, A. Barthelemy (UmPhy Thales)

Spectromicroscopy in a STEM

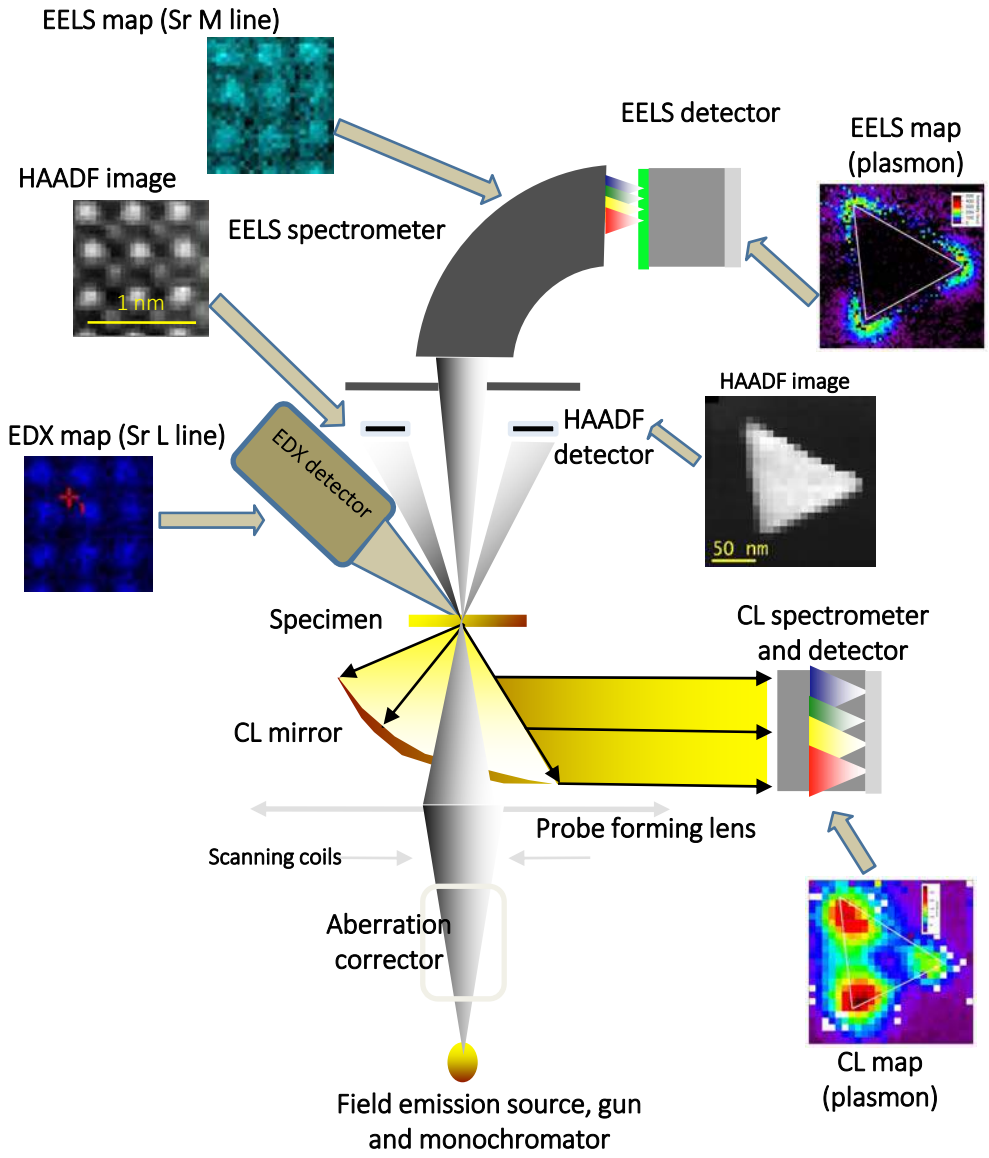

The multisignal approach

EELS spectroscopy : spectral domains

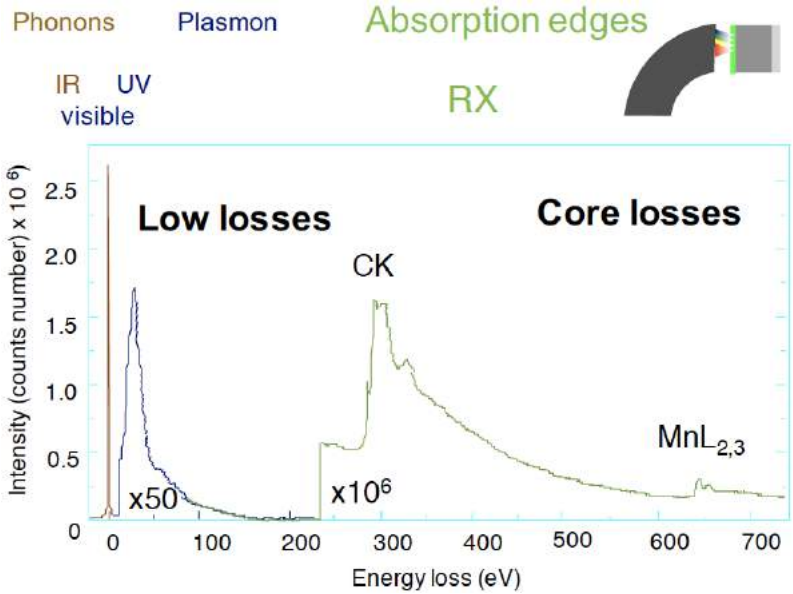

The spectrum image (hyperspectral) approach

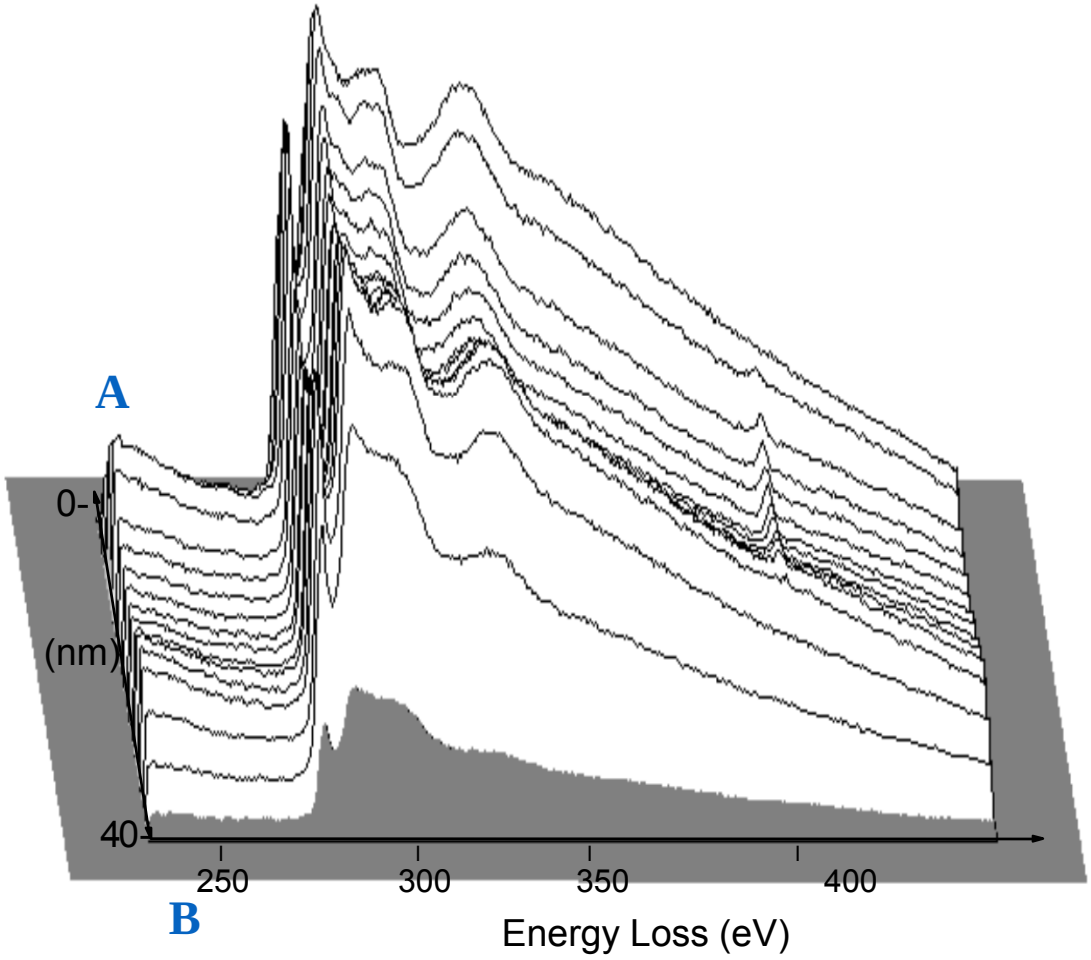

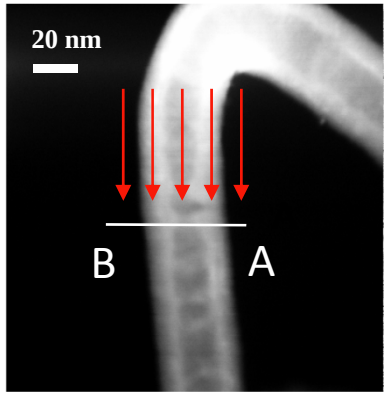

HAADF image

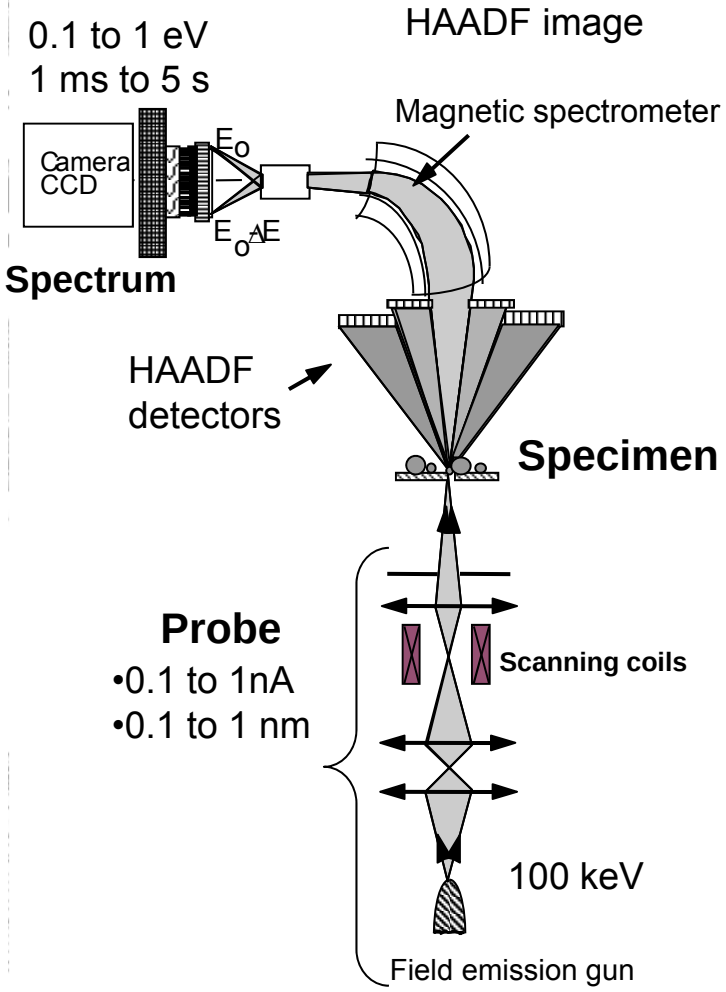

EELS: involved electron populations and associated transitions

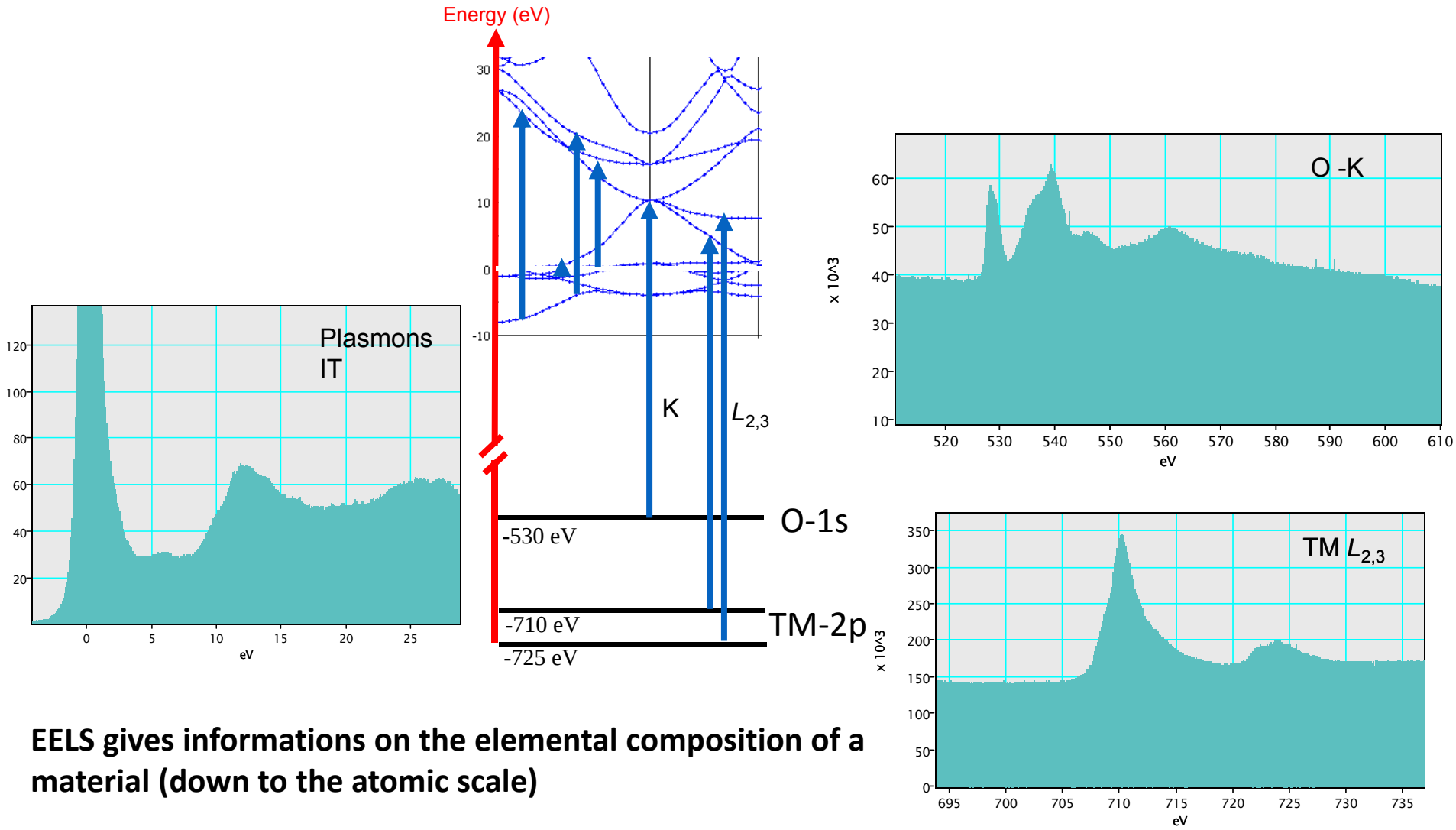

EELS gives informations on the elemental composition of a material (down to the atomic scale)

EELS gives informations on the electronic structure but it is usualy not a direct probe of the Ground State

Core-loss EELS Elemental analysis of PTO/STO superlattices

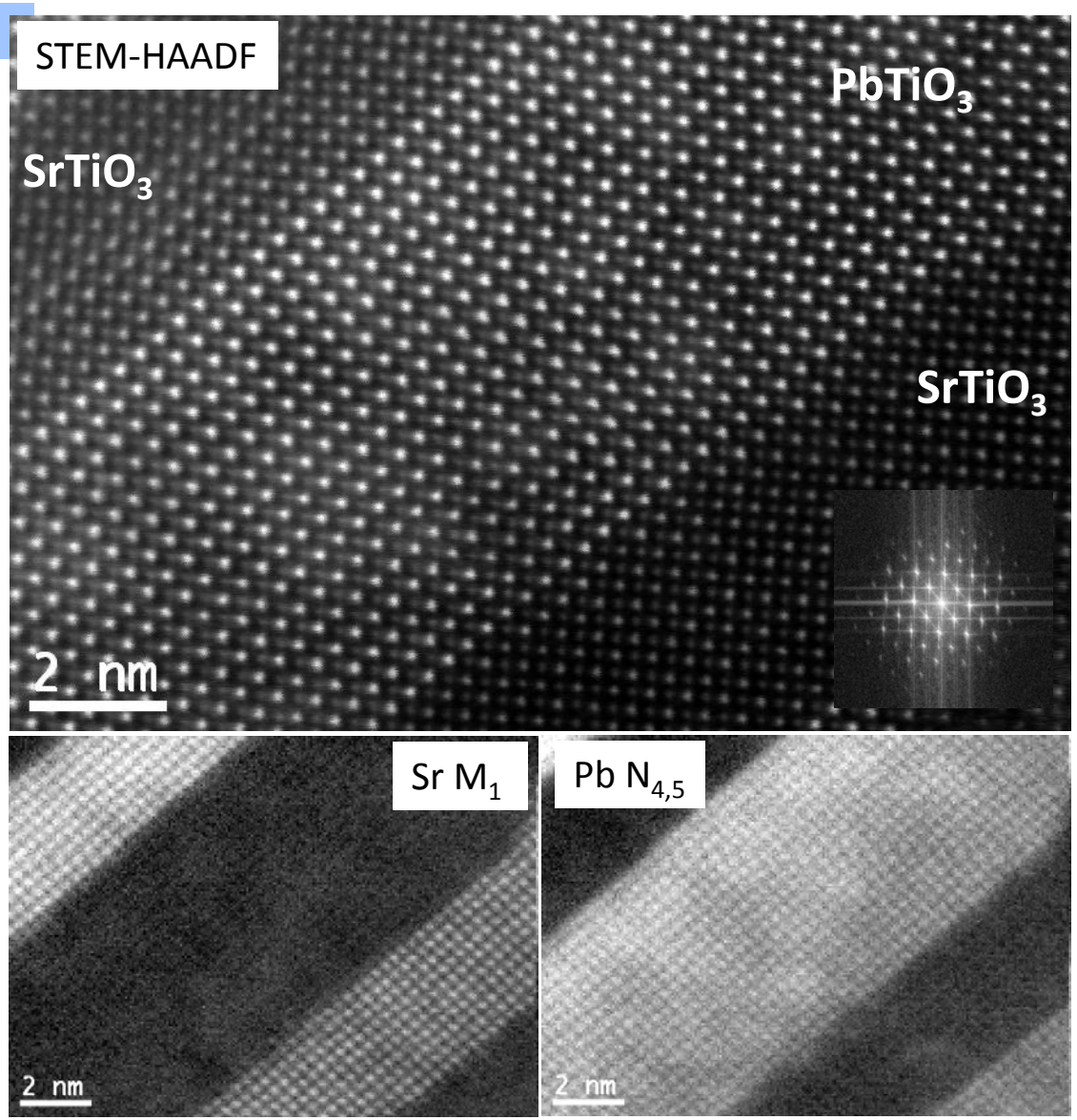

Negligible Sr-Pb interdiffusion in $SrTiO_3$-$PbTiO_3$ superlattices as evidenced by the EELS Sr M_1 (346-370 eV) and Pb $N_{4,5}$ (403-440 eV) signals.

STEM-HAADF, pixels size 9pm, 200 keV, 60pA, spots at 0.86 angstrom are seen in FFT.
STEM-EELS, pixel size 64pm, 5 ms per spectrum, 625 meV/ch, 200 keV, 60pA.

Courtesy K. March, A. Gloter, M. Kociak, M. Tence, A. Torres-Pardo (CNRS-Orsay-France); sample JM. Triscone (U. Geneva).

TM 2p edges (TiL2,3) : Origin of the peaks

Classic scheme for 3d orbitals crystal field splitting and 2p / L2,3 excitation

TiO_2

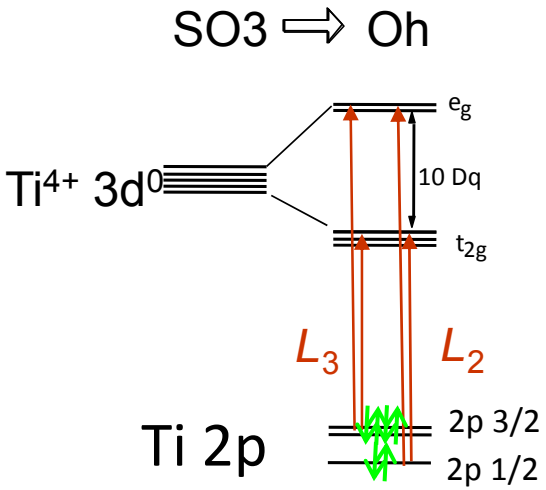

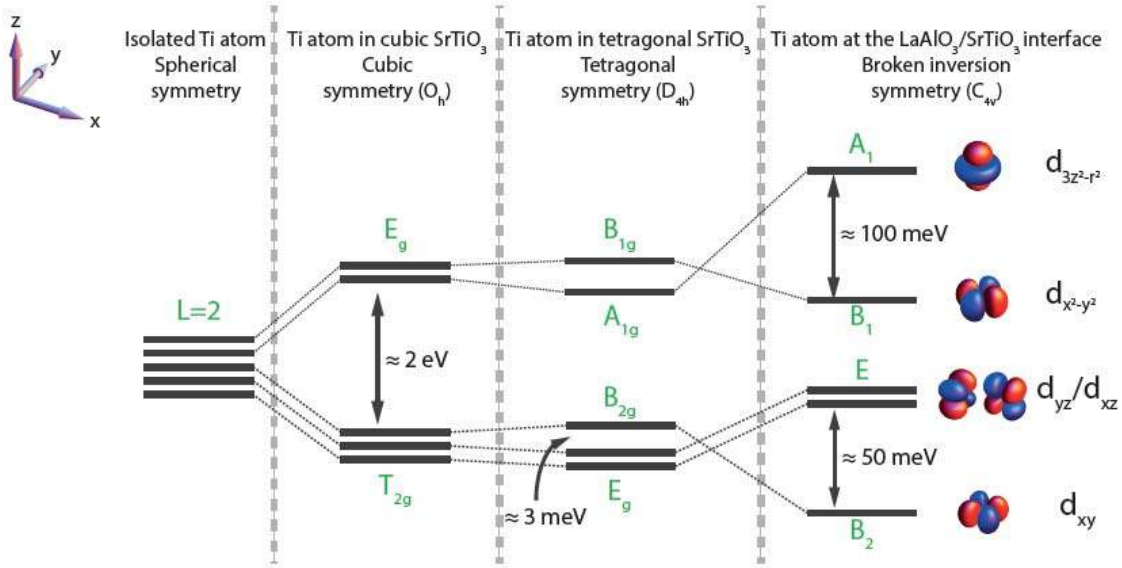

Figure 2.5: Energy of the Ti 3*d* orbitals in the presence of crystal field. Energy levels of the Ti 3*d* orbitals in a spherical, cubic, tetragonal and non inversion-symmetric tetragonal environment. The splittings were determined from experimental and theoretical studies [50–55]. The green labels refer to the irreducible representation to which the orbital(s) belong(s).

Measuring the crystal, field splitting across a $SrTiO_3$-$PbTiO_3$ interface by the EELS Ti $L_{2,3}$ edges fine structures evolution.

206x161 spim images, 50pm pixel size, 10 ms per spectrum, 90 meV/ch, 200 keV, 60pA, raw EELS data. Courtesy A. Gloter, M. Kociak, M. Tence, A. Torres-Pardo (CNRS-Orsay-France), sample JM. Triscone (U. Geneva).

A.Torres-Pardo et al., Phys. Rev. B 84, 220102 (2011).

P. Zubko et al. Nano Letters 12(6), 2846 (2012).

Coll. J.M. Triscone
U. Geneva

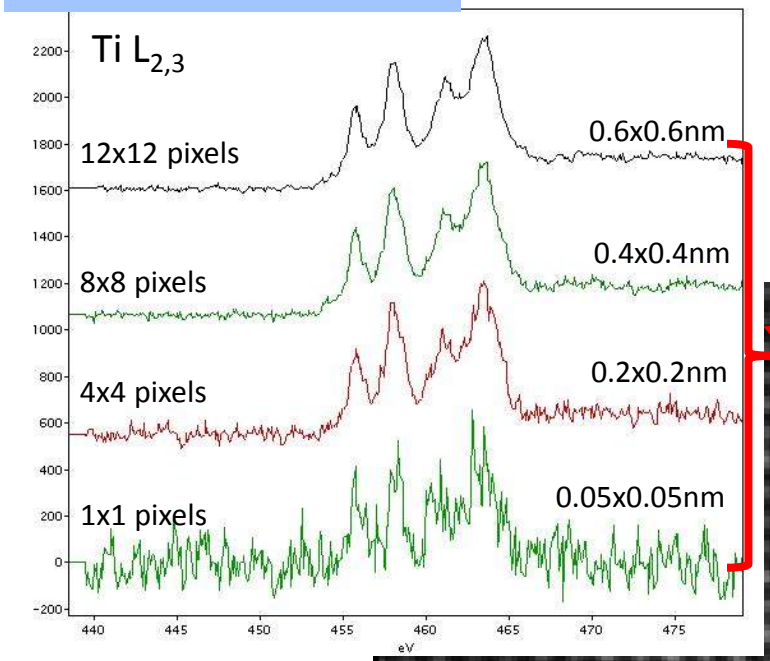

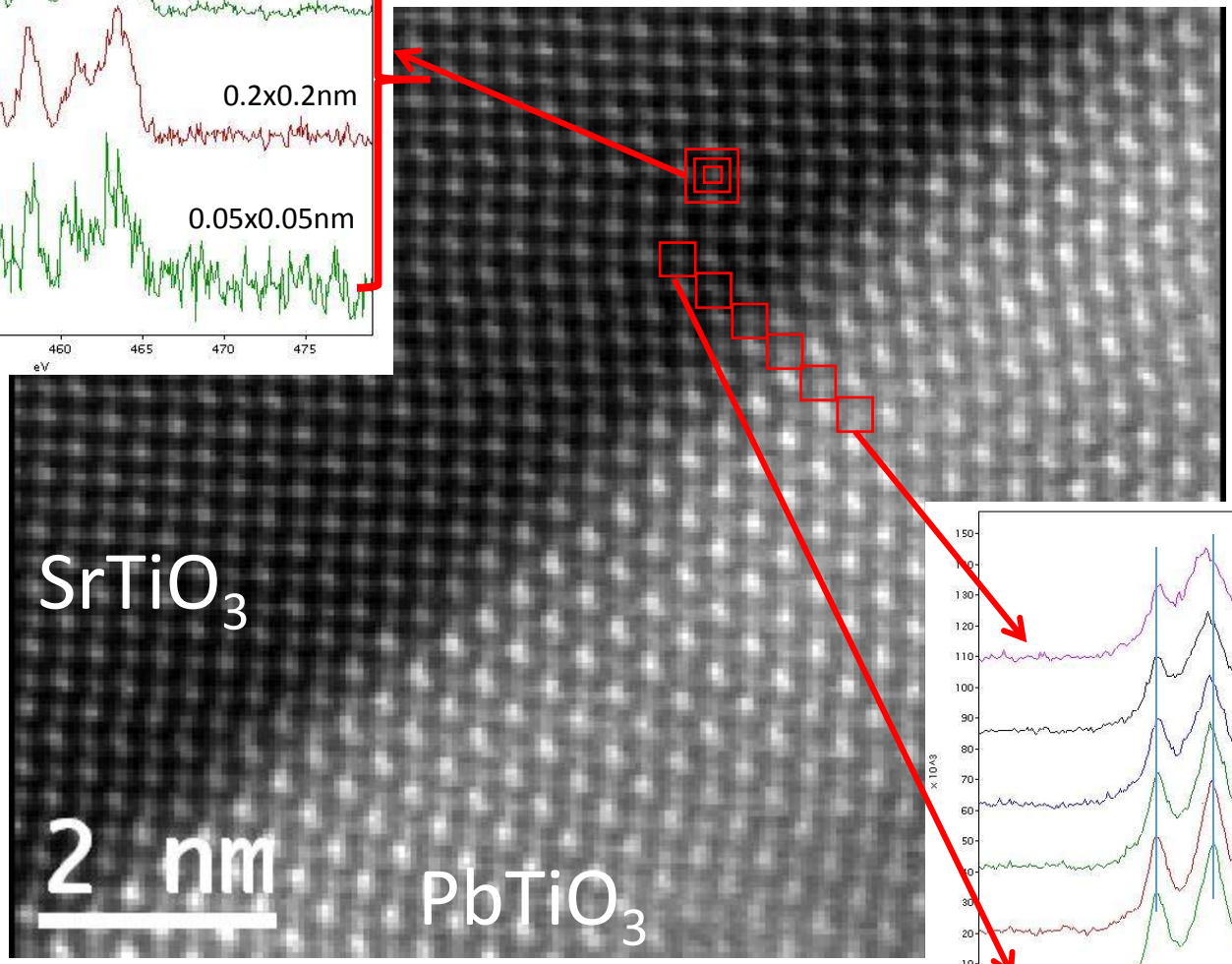

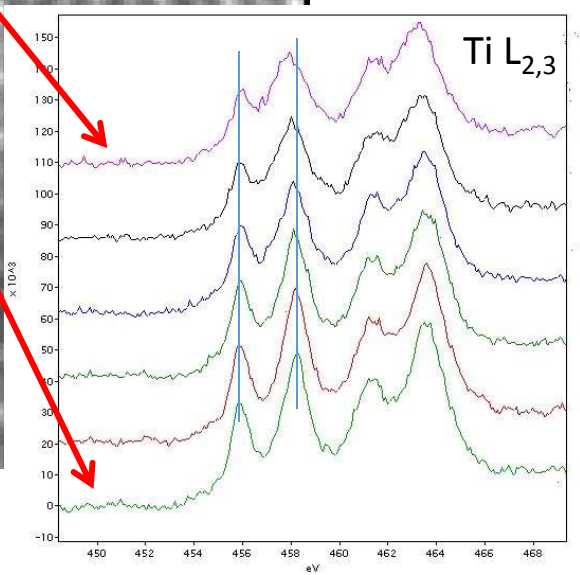

Spectromicroscopy up to 100.000 spectra

Unit cell resolved fine structures on Ti L2,3 edges

Structure and electronic structure of $LaNiO_3/LaMnO_3$ interfaces in superlattices

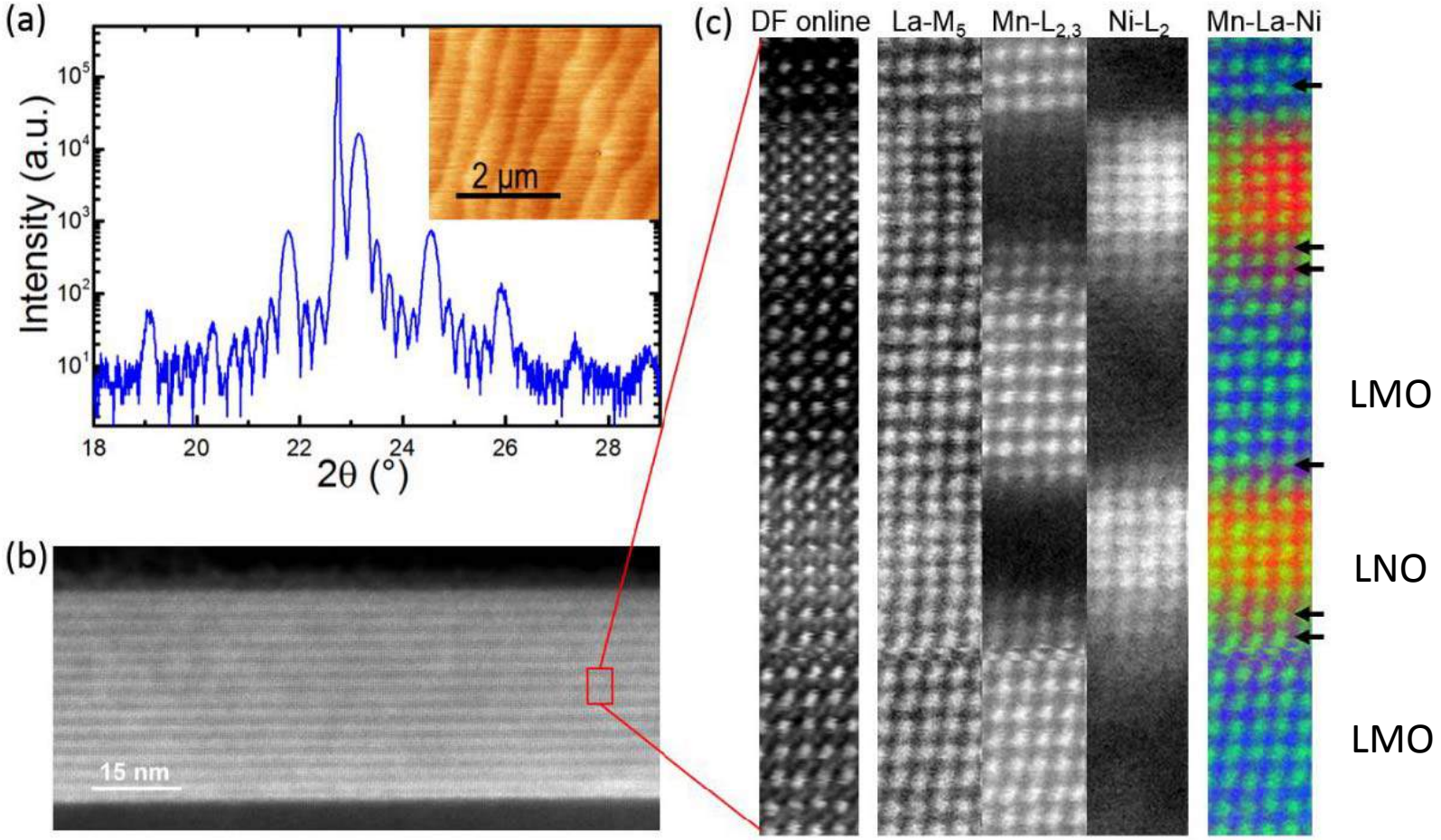

(a) XRD scans for a (8LNO/8LMO) 6 superlattice grown on (001)STO. Inset: corresponding atomic force microcopy image. (b) Low magnification TEM image. (c) EELS measurements showing the interfacial structural asymmetry (indicated by arrows).

Marta Guibert et al. Nanoletters (2015)

LMO/LNO interface is rougher compared to the LNO/LMO interface

Probing valence changes at $LaNiO_3/LaMnO_3$ interfaces

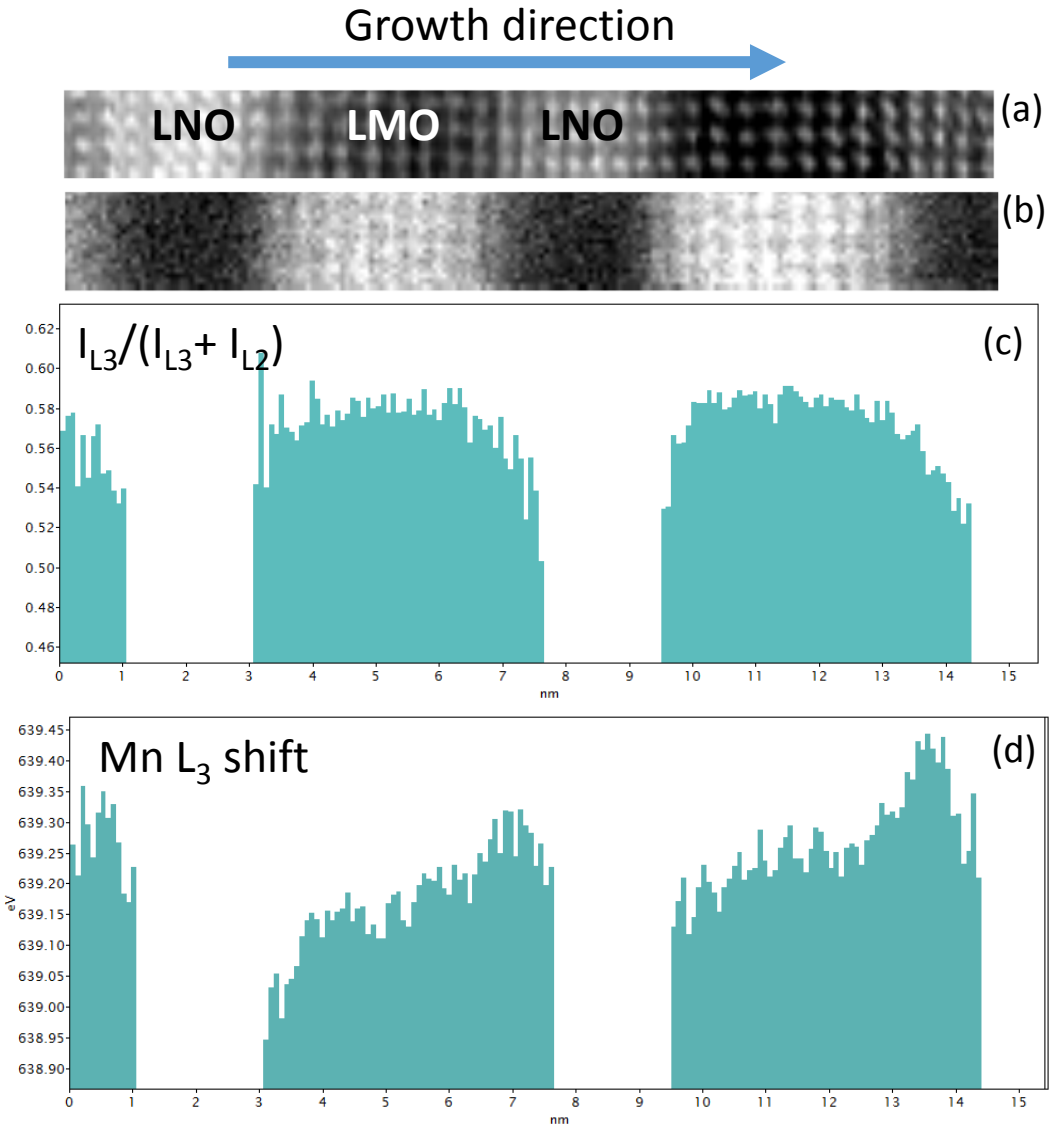

Interfacial charge transfer Mn^{3+}-Ni^{3+} towards Mn^{4+}-Ni^{2+}

Coll. J.M. Triscone U. Genève

Marta Guibert et al. Nano Letters 15, 7355 (2015)

Both energy shifts and branching ratio indicated introduction of more holes (Mn^{4+}) in the rougher LMO/LNO interface compared to the LNO/LMO interface

Charge quantification at interfaces, which sensitivity?

More Mn^{3+} at both interfaces and also in some part of the $CaMnO_3$ thin film, in link with superstructure due to oxygen vacancies ordering.

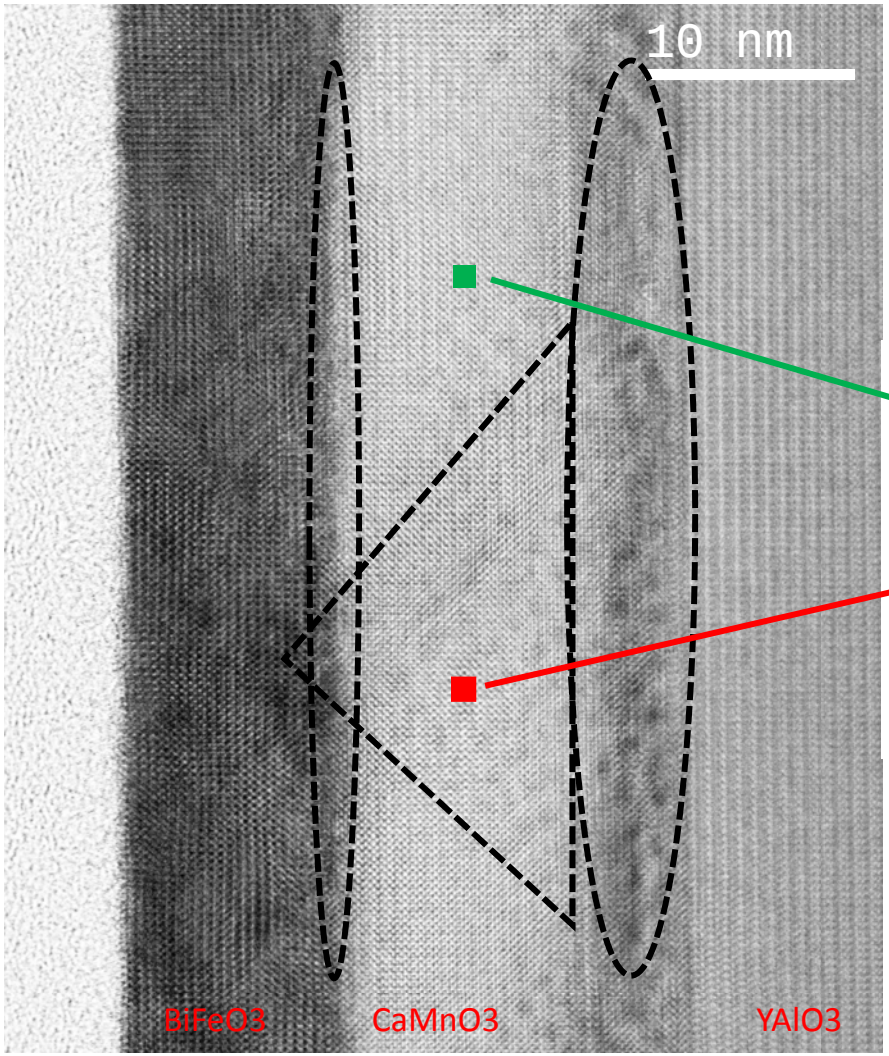

2 spectra from the central area of CMO with and without superstructure. Square surface is 1nm*1nm id est integration of 25 spectra

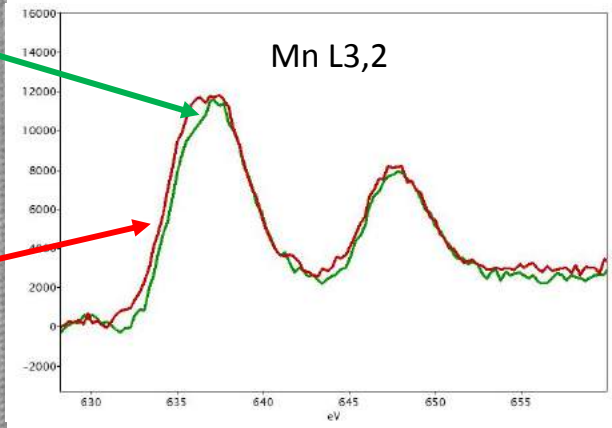

Coll. V. Garcia, S. Fusil, M. Bibes, A. Barthelemy (UmPhy Thales)

Charge quantification at interfaces, which sensitivity?

More Mn^{3+} at both interfaces and also in some part of the $CaMnO_3$ thin film, in link with superstructure due to oxygen vacancies ordering.

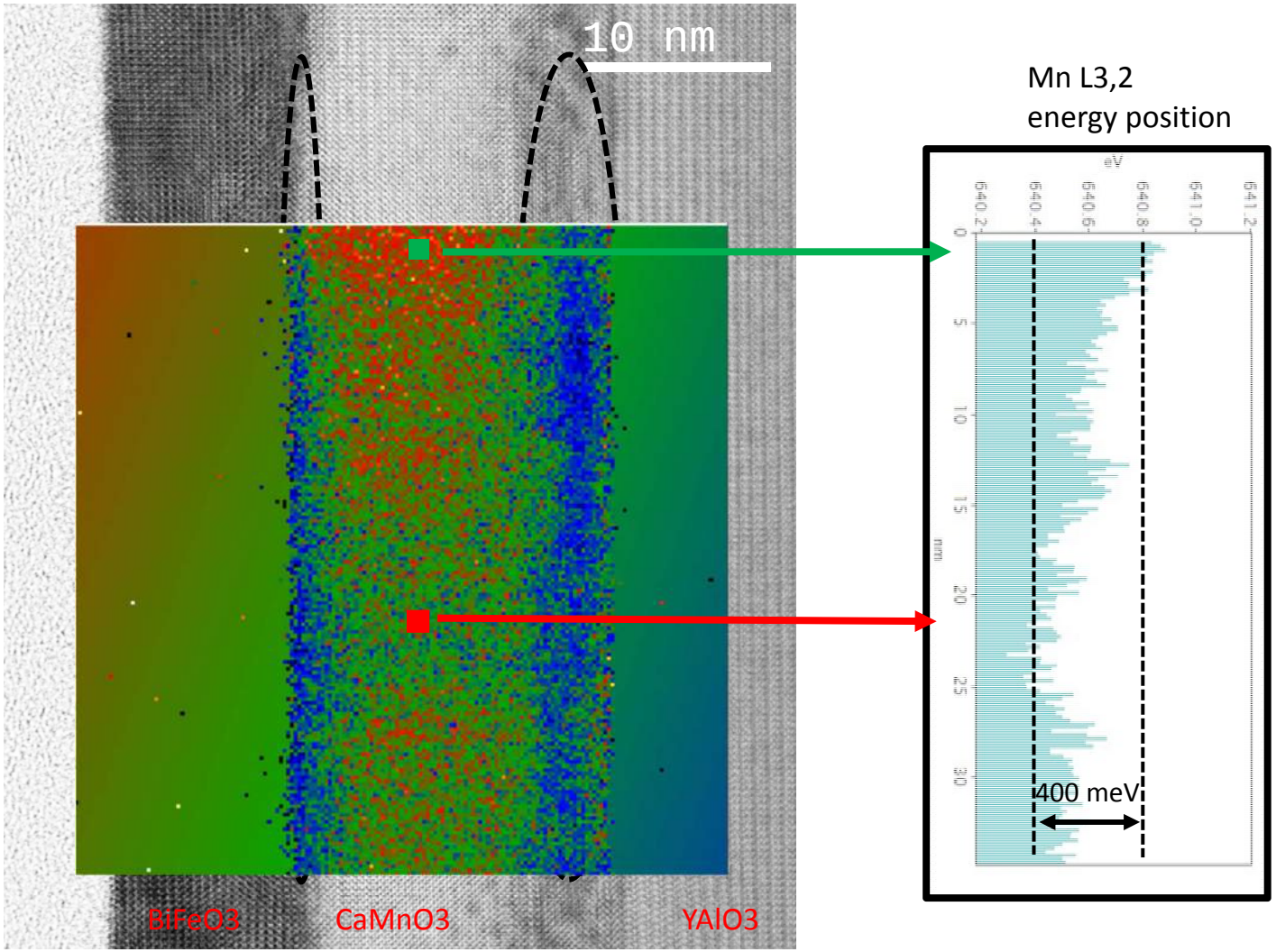

Coll. M. Bibes, V. Garcia, S. Fusil, A. Barthelemy (UmPhy Thales)

Charge quantification at interfaces, sensitivity down to a few 1/100 e-

Explorer la physique aux interfaces d'oxydes fortement corrélées: résultats récents et perspectives en microscopie électronique.

Alexandre Gloter et Odile Stephan (LPS, Université Paris-Sud, 91405 Orsay)

1. STEM imaging & EELS principles

1.1 A few generalities about transmission microscopy

1.2 Image formation principles in STEM and examples

1.3 EELS principles and examples

2. Application to oxide thin films

2.1. Strain relaxation in LAO/STO bi-interface

2.2. Oxygen octahedra rotation in LSMO

2.3. Textured VO2 thin film on sapphire

3. Few perspectives on STEM-EELS for oxides / interfaces studies

Strain engineering

refers to a general strategy employed in semiconductor manufacturing to enhance device performance. Performance benefits are achieved by modulating strain in the transistor channel, which enhances electron mobility (or hole mobility) and thereby conductivity through the channel.

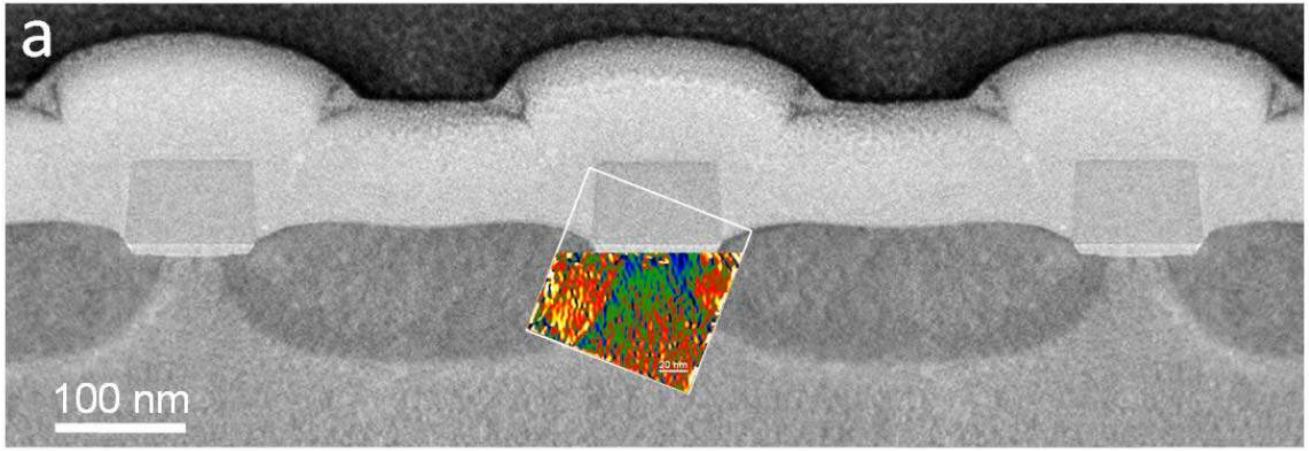

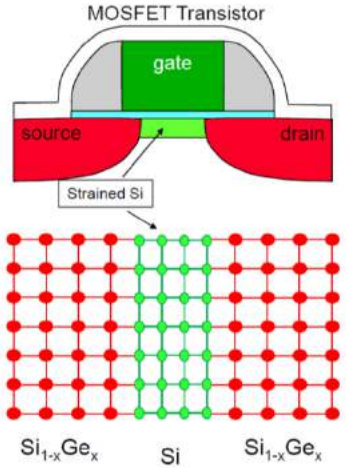

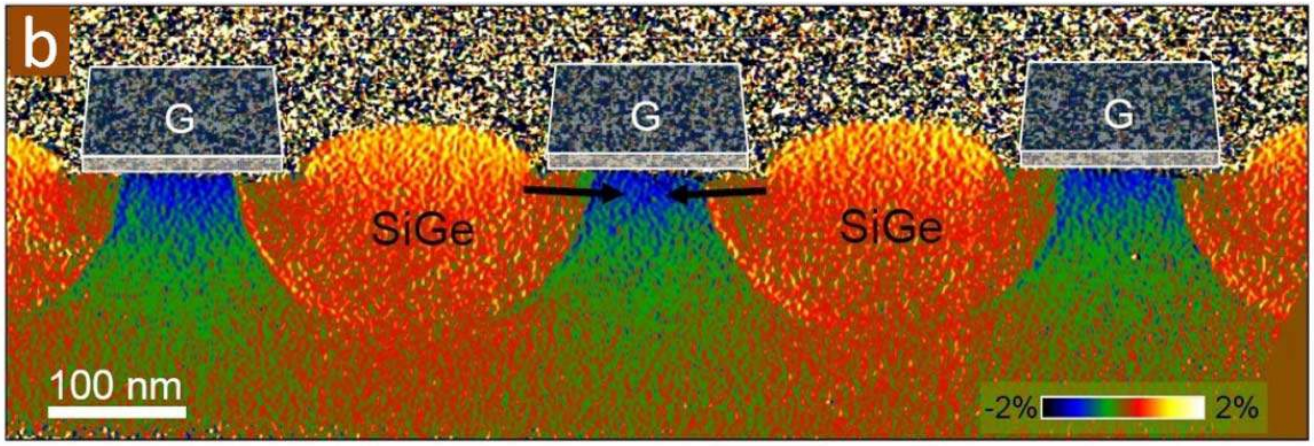

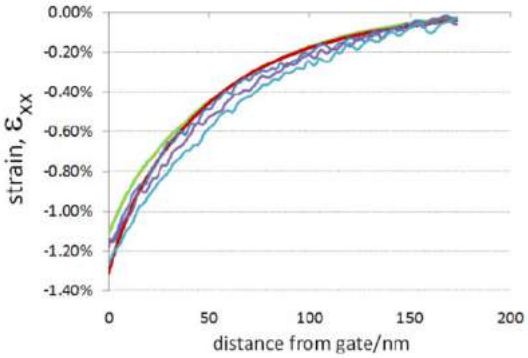

- Direct mapping of strain in a strained silicon transistor by high-resolution electron microscopy Hue, F; Hytch, M; Bender, H, et al. Phys. Rev. Lett. 100, 156602 (2008)
- Nanoscale holographic interferometry for strain measurements in electronic devices, Hytch M, Houdellier F, Hue F, et al. Nature 453, 1086 (2008)

SrTiO3/LaAlO3 bilayers : structure and dislocations

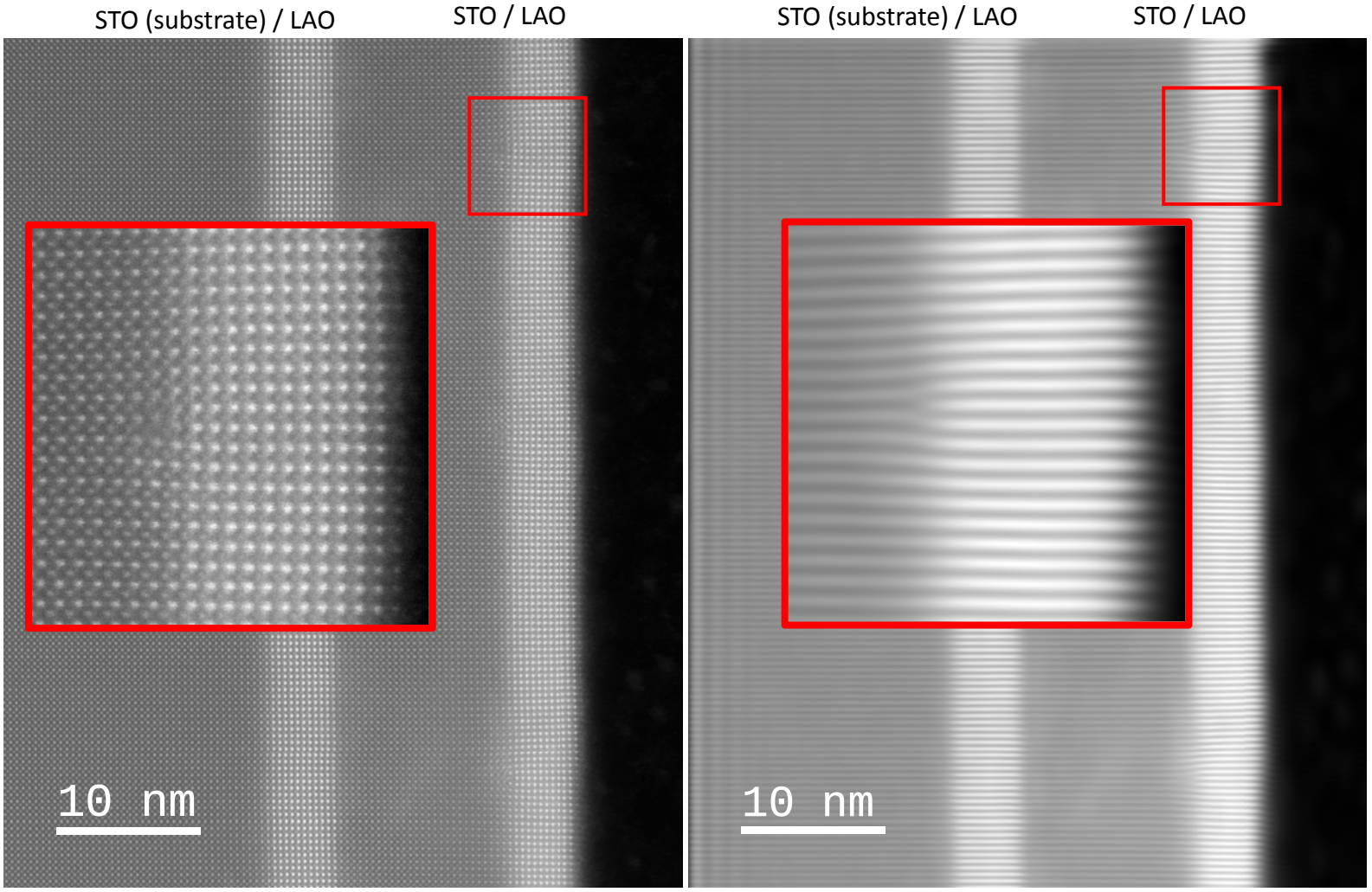

Collaboration (JM Triscone, U. Genève ; G. Tieri thesis)

$SrTiO_3$ unit cell (~3.90 Å) and $LaAlO_3$ pseudo cubic unit cell (~3.79 Å)
LAO should be 2.9 % tensile strained

Local tetragonality : c/a ratio mapping

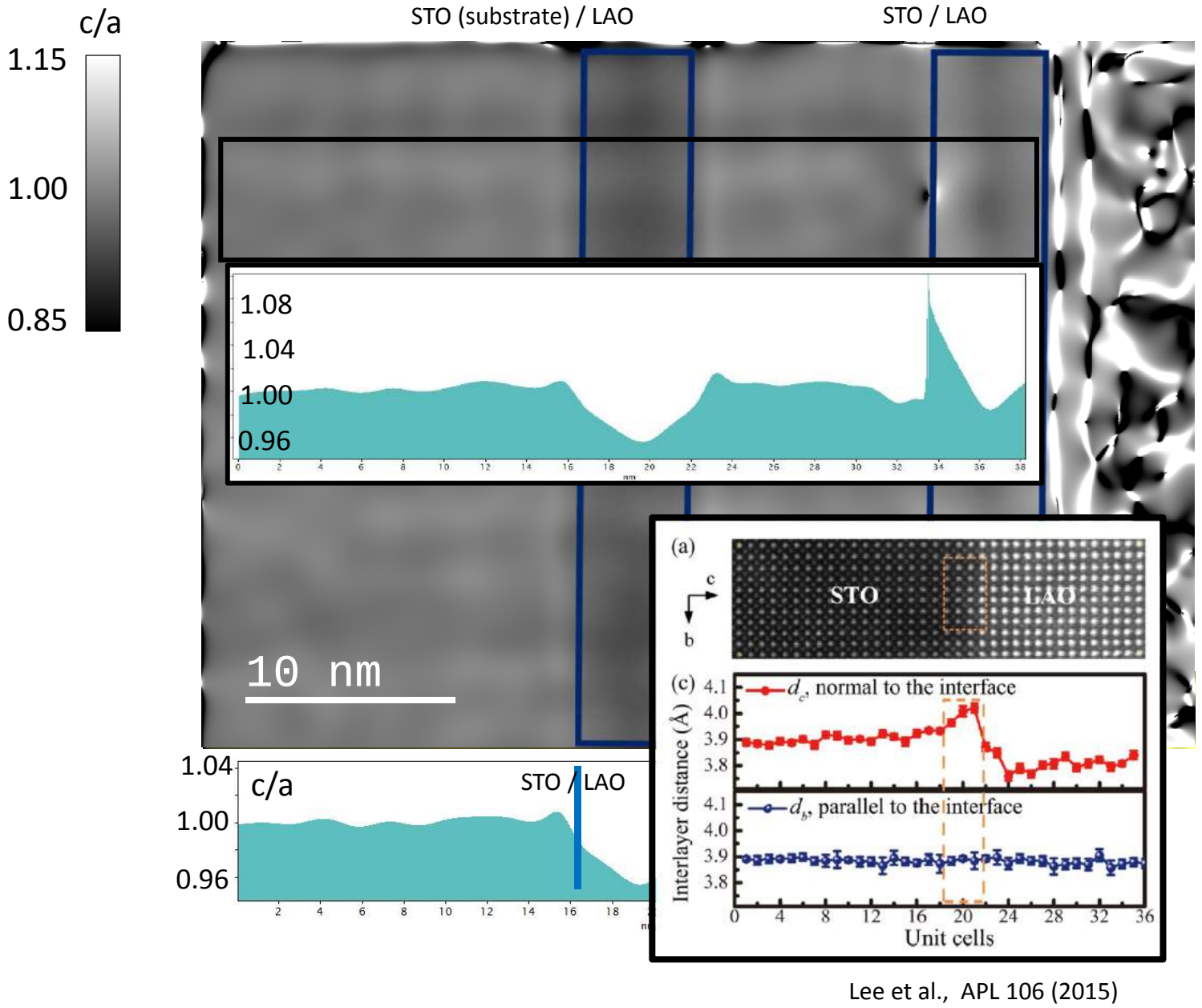

Lee et al., APL 106 (2015)

Orbitals hierarchy at the $LaAlO_3/SrTiO_3$ interface

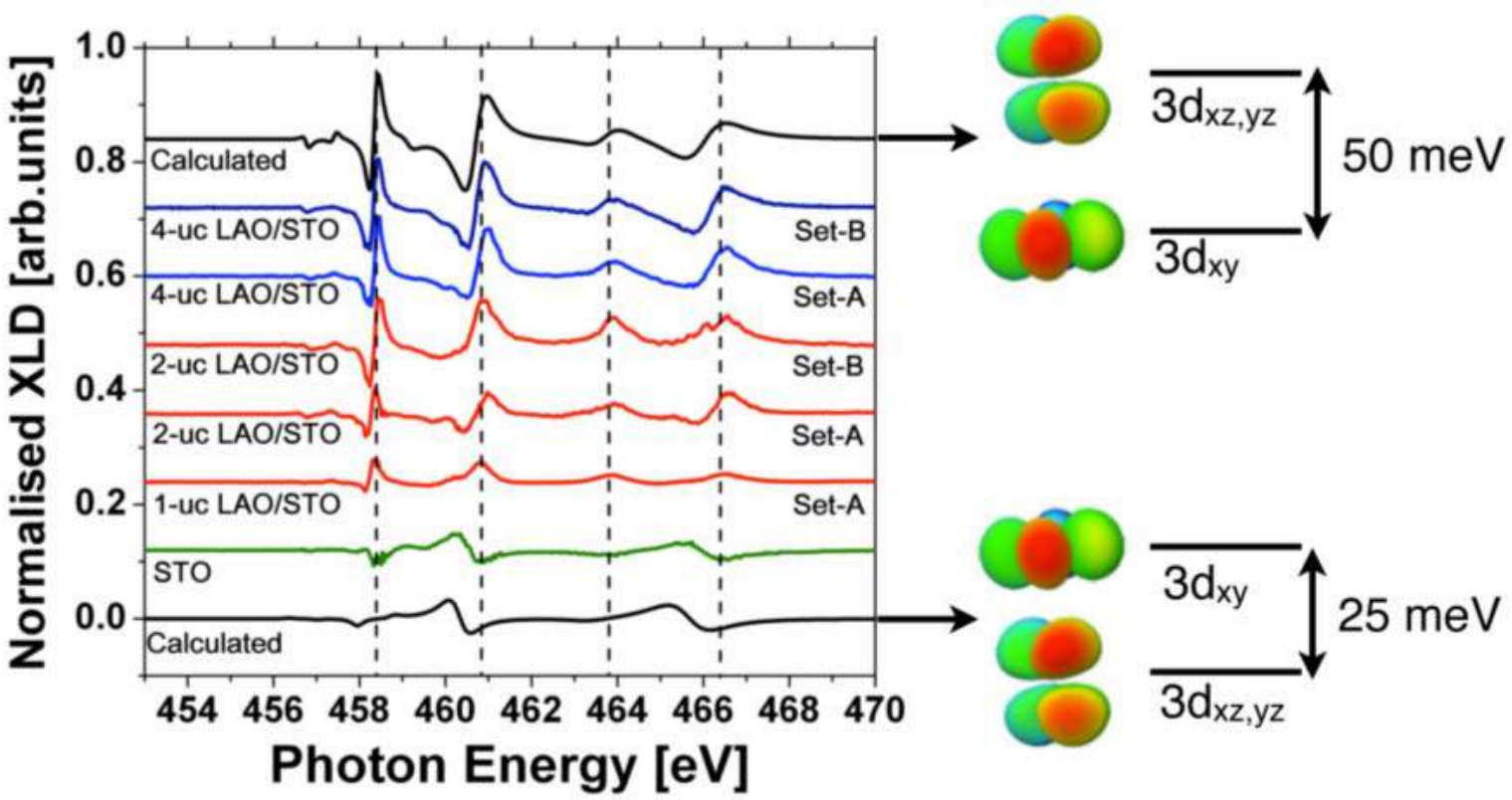

Figure 1. X-ray linear dichroism (XLD) spectra around the titanium $L_{2,3}$ absorption edge of $SrTiO_3$ (green line) and $LaAlO_3/SrTiO_3$ bilayers characterised by a $LaAlO_3$ thickness below (red lines) and above (blue lines) the critical thickness of four unit cells. Data from two sample sets are shown. Black lines are calculations which reproduce the data on STO (bottom) and LAO/STO (top) using multiplet atomic model calculations with point charge crystal field. On the right a schematic of the orbital splitting needed to reproduce the data is depicted, showing the inversion of hierarchy between in-plane and out-of-plane t_{2g} orbitals at the $LaAlO_3/SrTiO_3$ interface.

Salluzzo et al. PRL 102, 166804 (2009)

XAS isotropic and EELS comparison

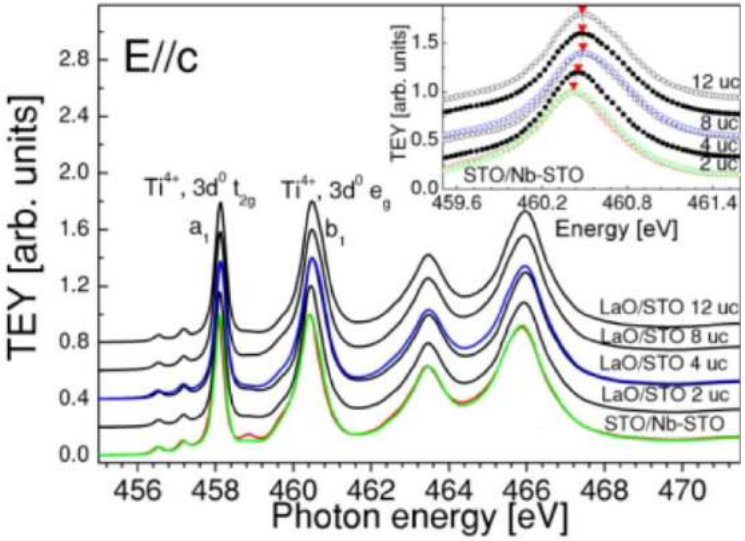

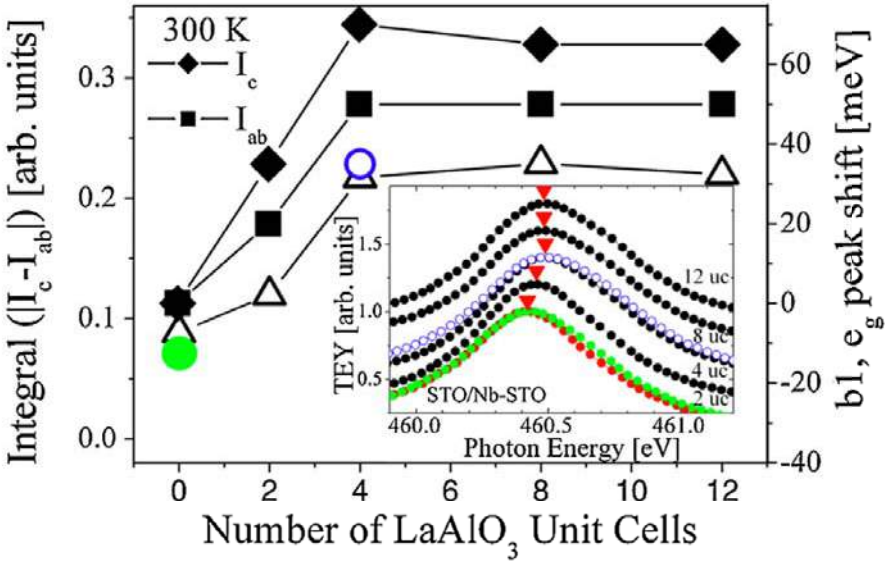

Salluzzo et al. PRL 102, 166804 (2009)

STO (substrate) / LAO

STO / LAO

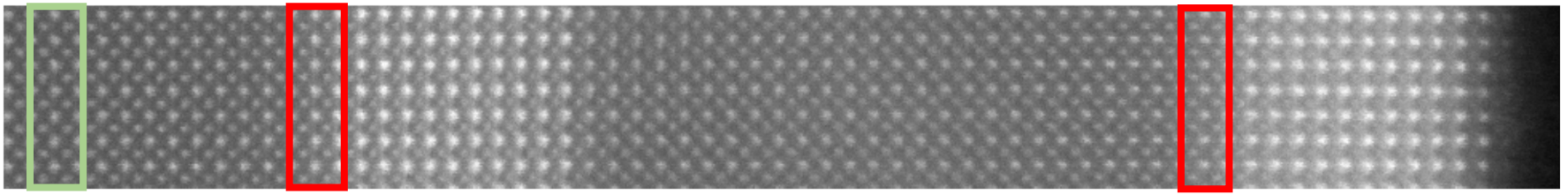

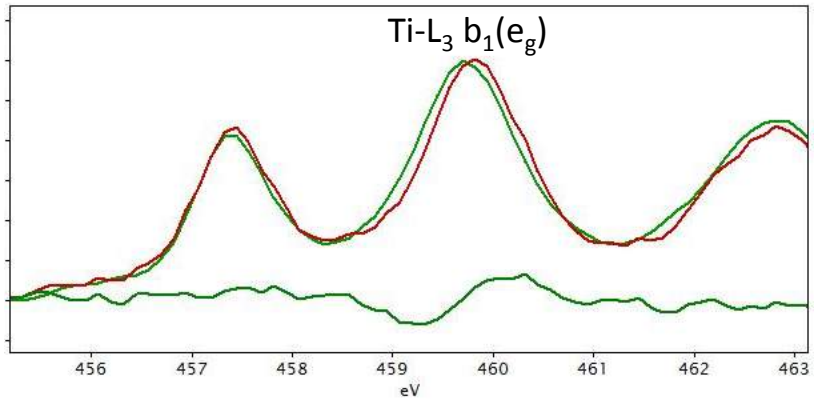

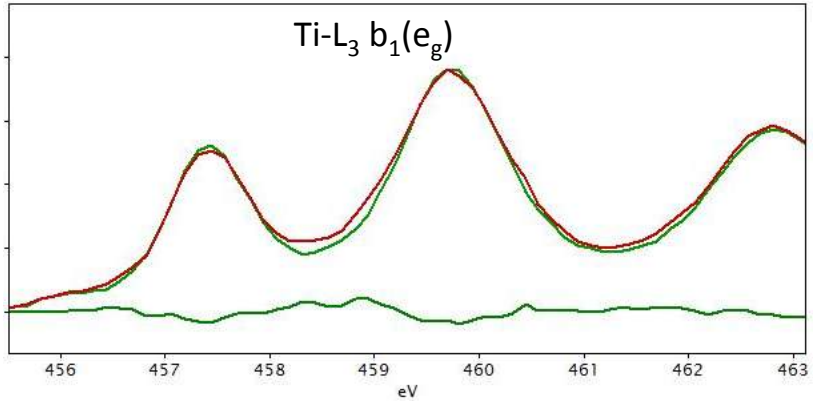

Ti-L_3 $b_1(e_g)$ shift, tetragonality and dislocation on STO-LAO bi-interface

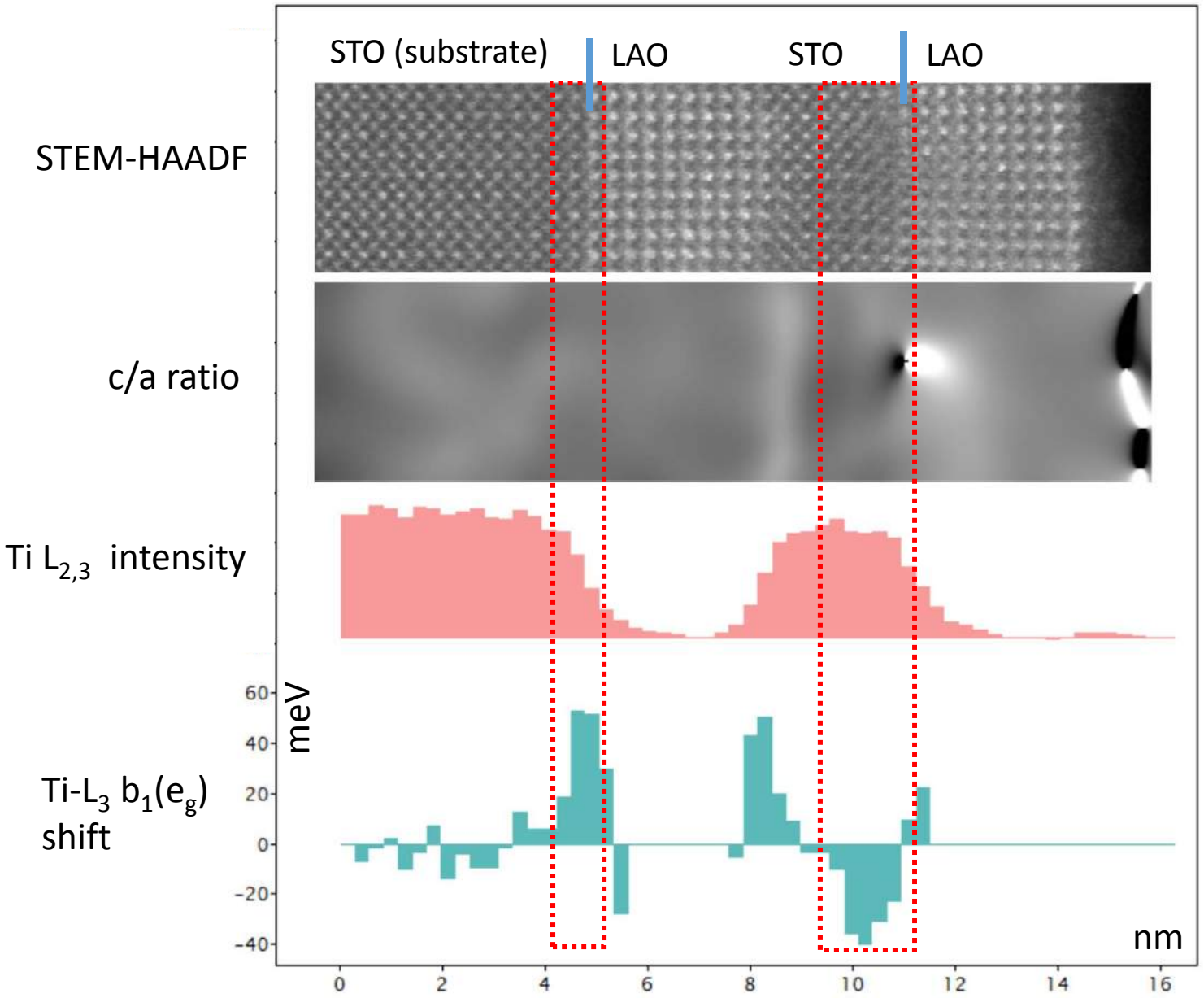

Strain relaxation in LAO/STO bi-interface

Degeneracy lifting of the t2g and eg at the interface have been attributed and related to distortion, spin-orbit, quantuum well confinement, hopping term changes, numbers of electrons in the well, ……

Here we report possible role of dislocation (via disortion evolution) into orbital reordering. Degeneracy lift might be smaller and inhomogneous at the STO(film)-LAO(film) interface.

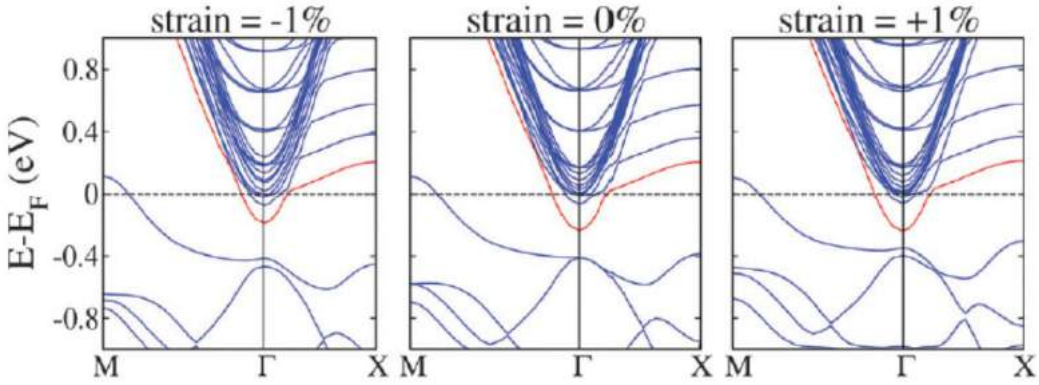

Role of strain or interface reconstruction on degeneracy lifting of the t2g have been reported by DFT.

Betash et al. PCCP 18, 6831 (2016)

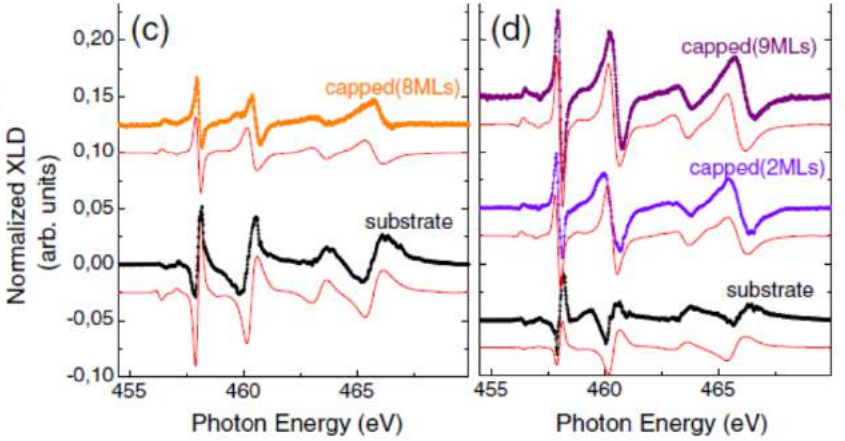

A major drawback of STEM-EELS is to be mostly isotropic (equivalent of XLD is difficult to achieve at nanometer resolution). So no formal evidence that shift is related to a symmetry breaking.
Work in progress….

Hierachy inversion have been reported for LAO(110)/STO(110) by XLD
Pesquera et al. PRL 113, 156802 (2014)

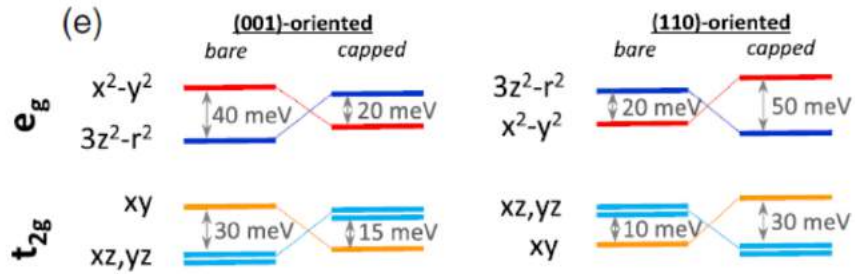

Oxygen octahedra rotation in LSMO

Perovskite oxygen octahedra tilt and Glazer notation

$a^oa^oa^o$ (Pm3m)

$a^oa^oc^+$ (P4/mbm)

$a^oa^oc^-$ (I4/mcm)

$[010]_{pc}$ [100]pc

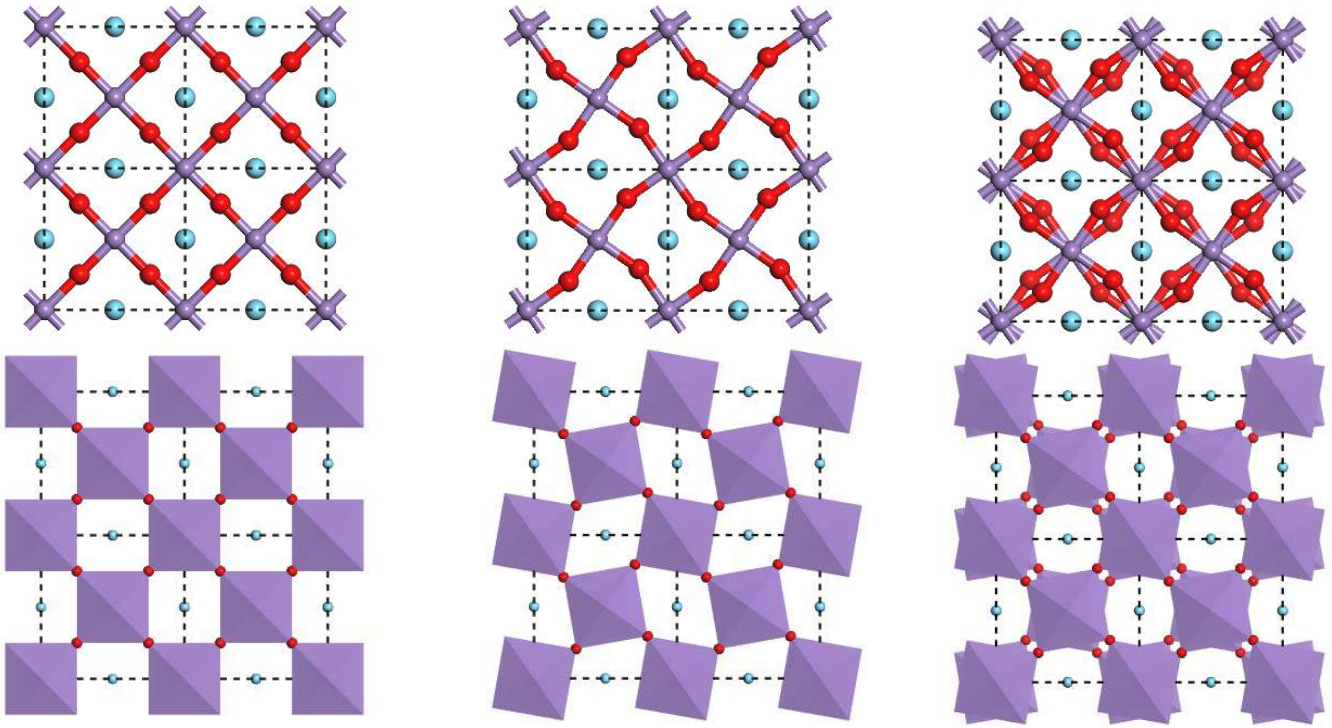

Tilt around c is 10°

[001]pc zone axis

Oxygen octahedra rotation in LSMO

$(La_{1-x},Sr_x)MnO_3$ has octahedra tilt over several axis $a^-a^-c^+$ (Pnma)

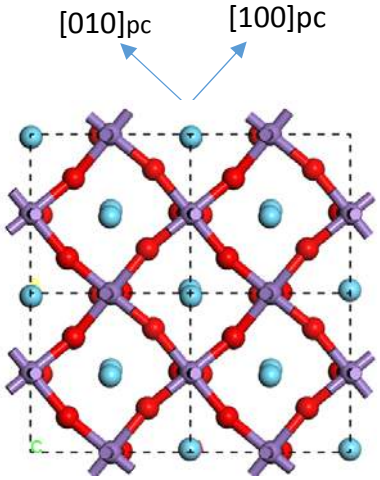

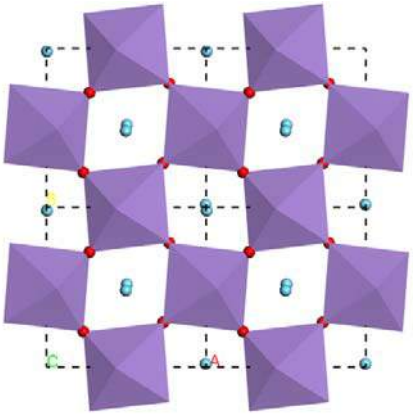

It is in phase rotation around c

[001]pc zone axis

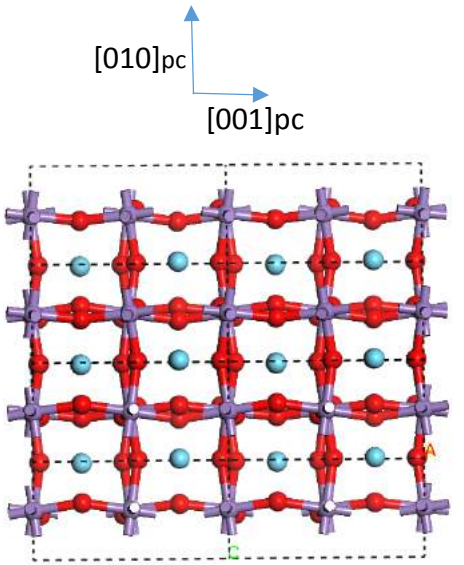

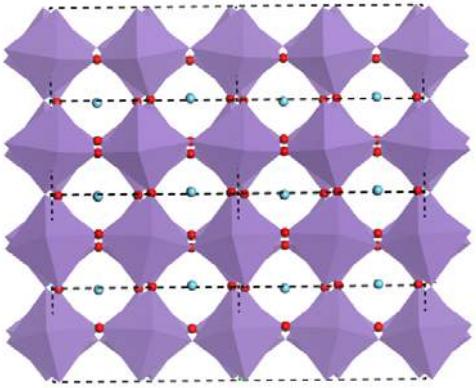

It is out of phase rotation around a (and b)

[100]pc zone axis

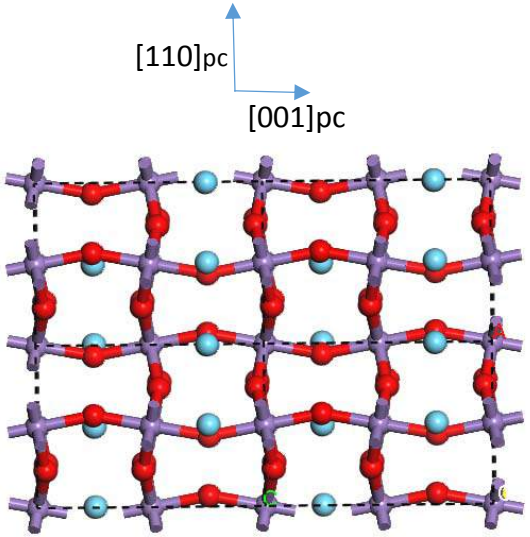

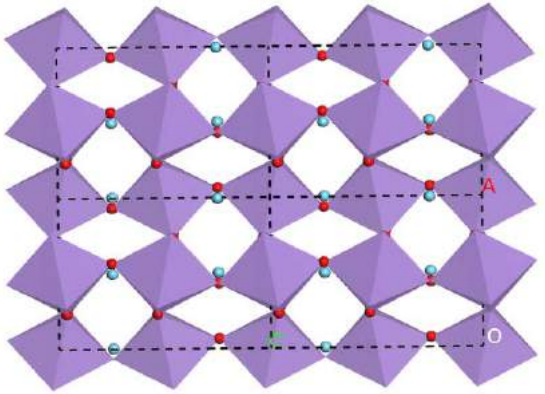

Octahedra rotations induce zig-zag chain visible along

[1-10]pc zone axis

Oxygen octahedra rotation in LSMO

STEM-ABF imaging of $(La_{1-x},Sr_x)MnO_3$

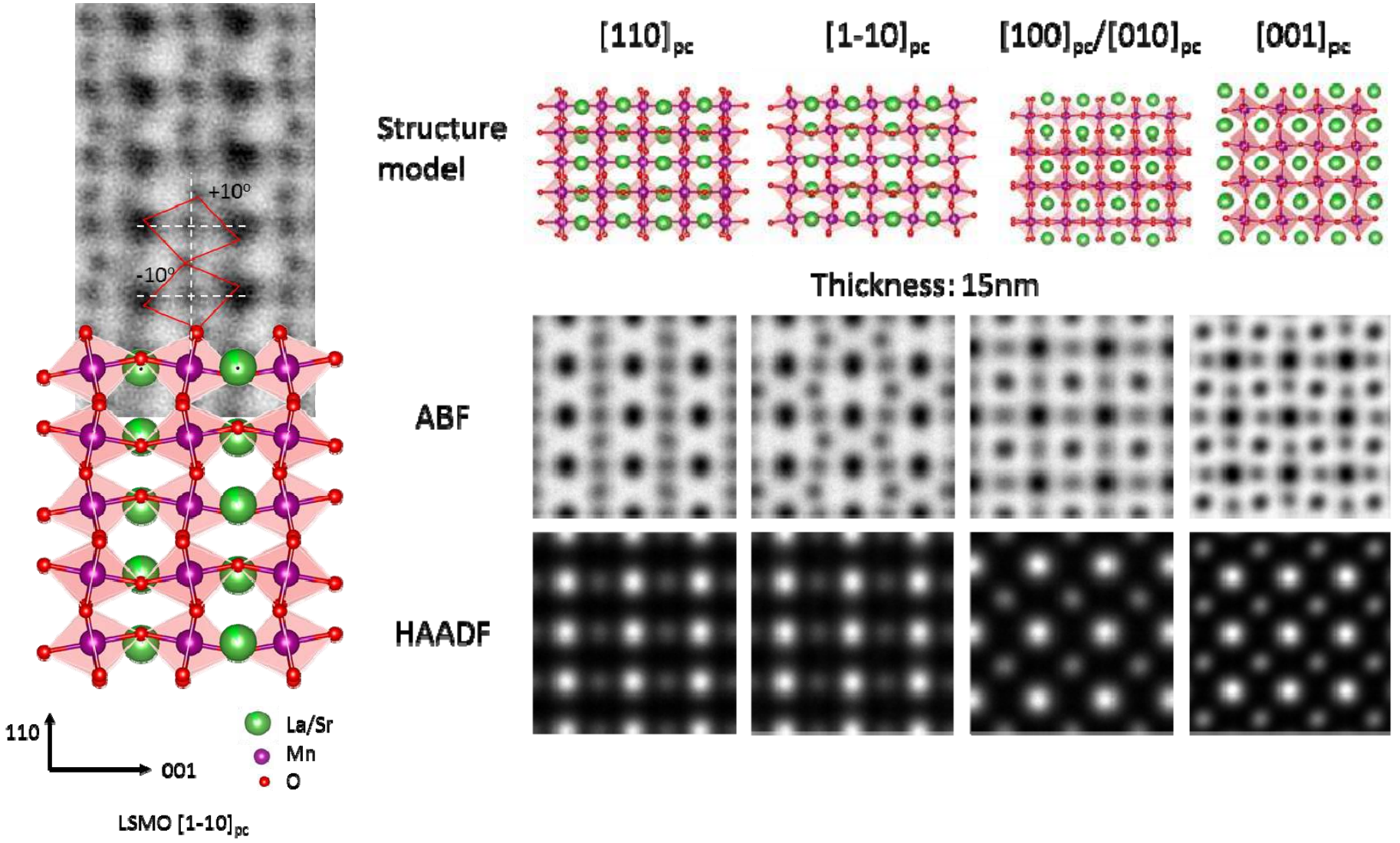

Li et al. Scientific Reports **7**, 40068 (2017)

Oxygen octahedra rotation in LSMO

Towards 3D Mapping of BO_6 Octahedron Rotations at Perovskite Heterointerfaces, Unit Cell by Unit Cell

[110]pc axis

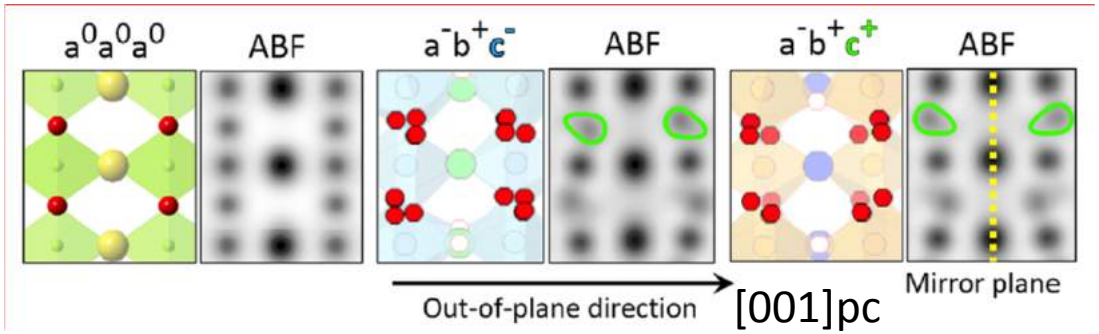

Figure 2. Qualitative 3D determination of BO_6 rotation. Atomic models and corresponding ABF images (multislice simulation using Kirkland's code[37]) of model ABO_3 perovskite structures (modeled using POTATO[38]) with (a) $a^0a^0a^0$, (b) $a^-b^+c^-$, and (c) $a^-b^+c^+$ BO_6 rotation patterns, viewed from a $[110]_{pc}$ direction. The $[001]_{pc}$ is set to be the out-of-plane direction, shown as the black arrow. The alignment of oxygen atoms in this projection depends on the BO_6 rotation pattern of the structure. Oxygen columns in the corresponding simulated ABF images are therefore no longer round but have a teardrop-like shape (outlined in green in (b) and (c)), providing 3D information about the BO_6 rotation. For example, the presence of a "+" rotation in the out-of-plane direction can be seen as a mirror plane (yellow dashed line in (c)) emerging between two adjacent oxygen columns.

He et al. ACS **8** 2015

[110]pc axis

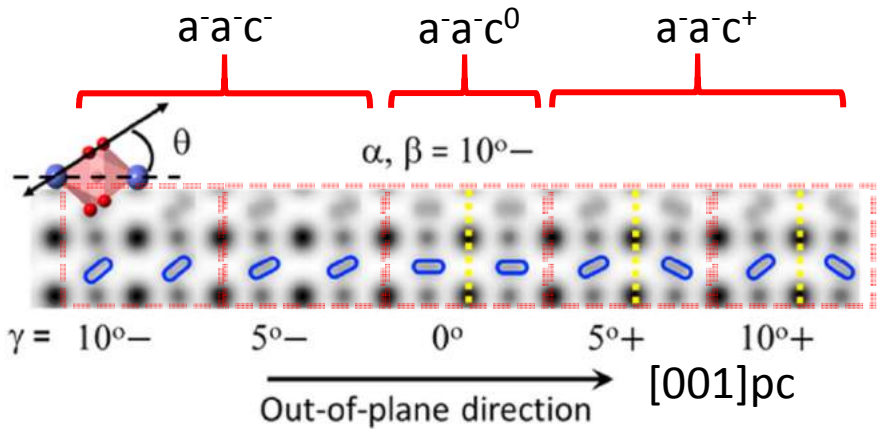

Figure 3. Quantitative 3D determination on BO_6 rotation. Simulated ABF image chart of model perovskite structures with BO_6 rotations of constant α and β but different γ. The $[001]_{pc}$ is set to be the out-of-plane direction. The overlapped polyhedral model highlights the position of oxygen columns (red) in the simulated images. The resultant oxygen column image can be considered as an ellipse (outlined in blue), due to α and β rotations both being "–". We can define an inclination angle θ between the major axis of the ellipse with respect to a reference (e.g., A–A or B–B). In this case, the magnitude of θ has a correlation with the magnitude of the γ rotation, and therefore quantitative information can be obtained by measuring θ. Yellow dashed lines indicate the mirror planes along the out-of-plane direction when γ rotation is either "+" or "0". A more detailed summary of shape analysis can be found in the Supporting Information.

Oxygen octahedra rotation in LSMO

How interface deals with different rotation ?

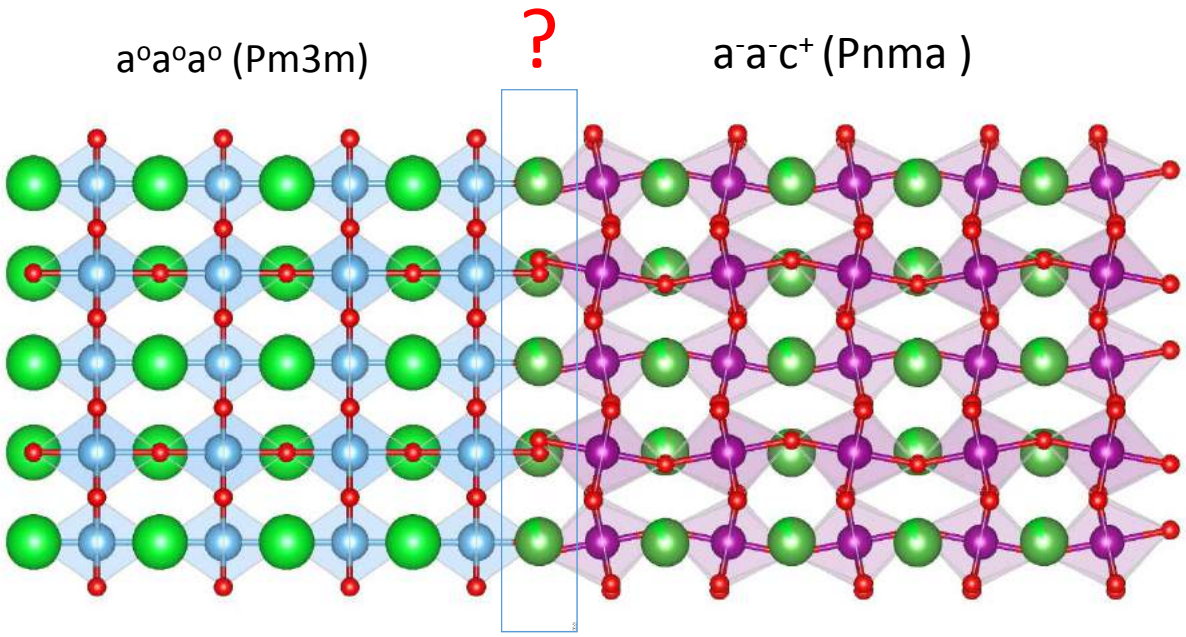

(LSMO-STO)/STO Mismatch of lattice=(3.875-3.905)/3.905=-0.77%

Mismatch of oxygen octahedra rotation=(170-180)/180=5.6% ???

Oxygen octahedra rotation in LSMO

LSMO / STO superlattices

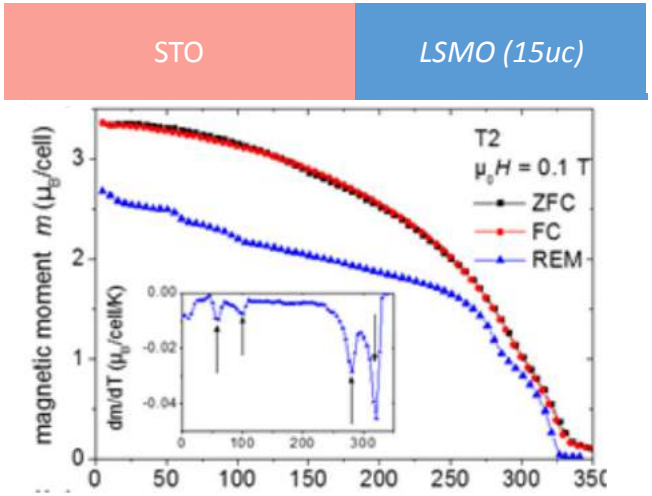

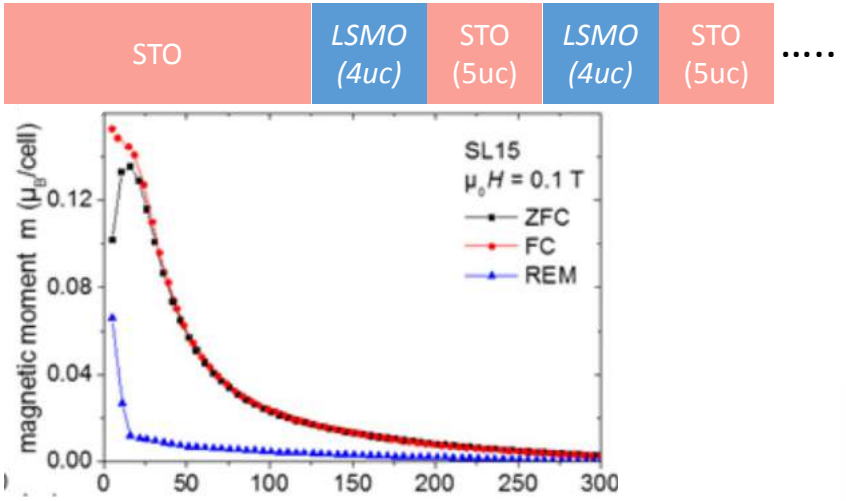

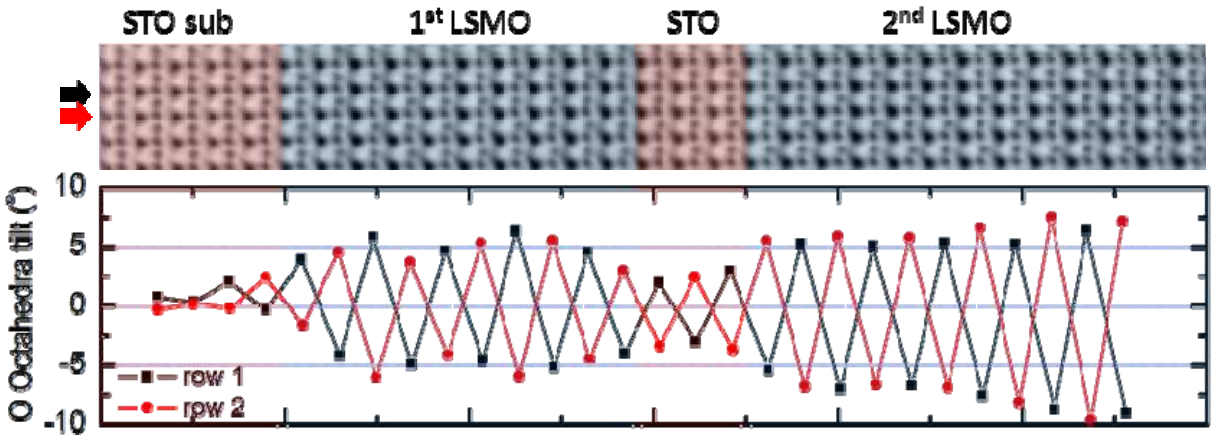

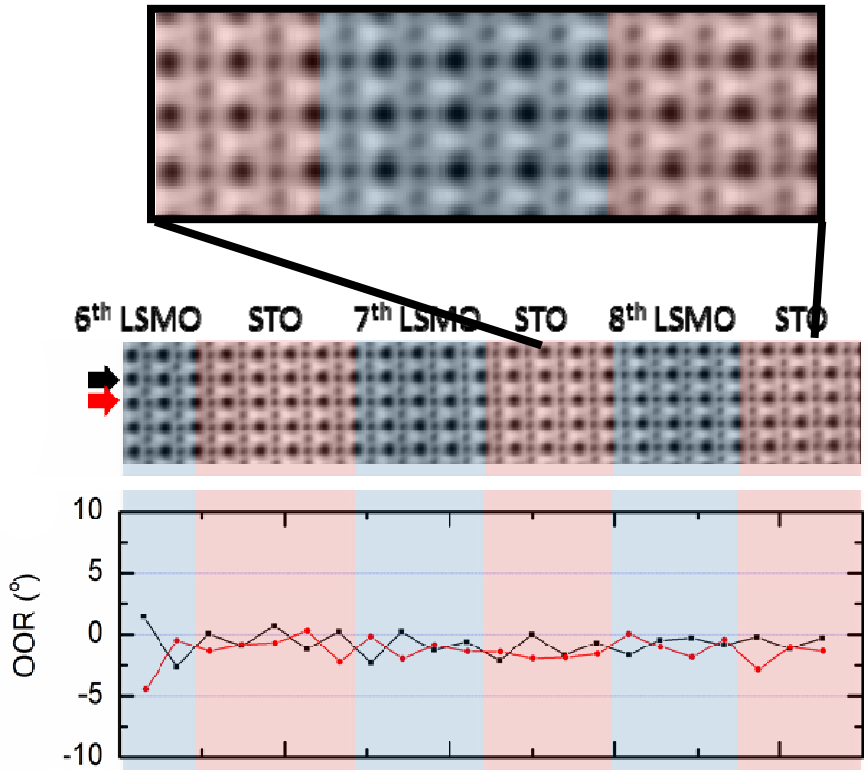

Li et al. Scientific Reports **7**, 40068 (2017)

Oxygen octahedra rotation in LSMO

Tuning magnetic anisotropy by interfacially engineering the oxygen coordination environment in a transition metal oxide

Daisuke Kan[1]*, Ryotaro Aso[1], Riko Sato[1], Mitsutaka Haruta[1], Hiroki Kurata[1] and Yuichi Shimakawa[1,2]

Impact of interfacial coupling of oxygen octahedra on ferromagnetic order in $La_{0.7}Sr_{0.3}MnO_3/SrTiO_3$ heterostructures

Xiaoyan Li[1,2], Ionela Lindfors-Vrejoiu[3], Michael Ziese[4], Alexandre Gloter[2] & Peter A. van Aken[1]

Controlled lateral anisotropy in correlated manganite heterostructures by interface-engineered oxygen octahedral coupling

Z. Liao[1], M. Huijben[1]*, Z. Zhong[2], N. Gauquelin[3], S. Macke[4,5], R. J. Green[4,6], S. Van Aert[3], J. Verbeeck[3], G. Van Tendeloo[3], K. Held[2], G. A. Sawatzky[4], G. Koster[1] and G. Rijnders[1]

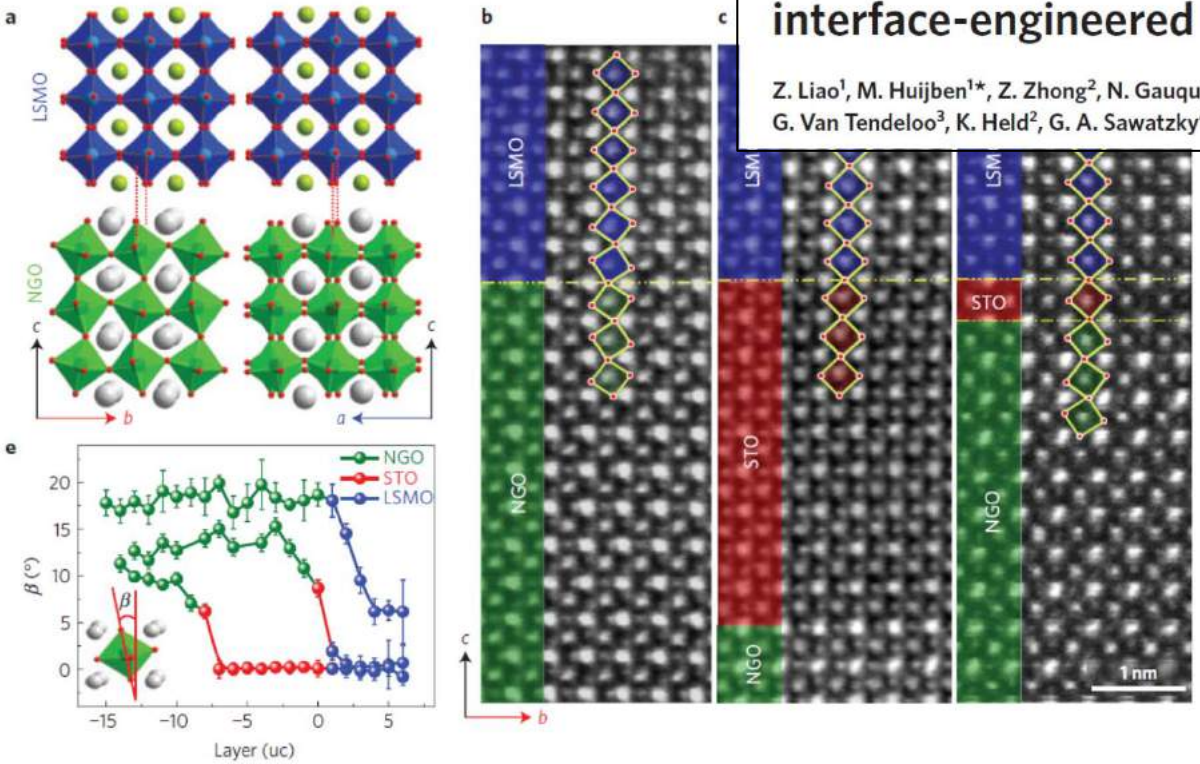

Figure 1 | Oxygen octahedral coupling at interfaces in manganite heterostructures. a, Schematic models of atomic ordering in LSMO and NGO crystal structures. **b–d**, Inversed annular bright-field STEM images of LSMO/NGO (**b**), LSMO/STO (9 uc)/NGO (**c**) and LSMO/STO (1 uc)/NGO (**d**) heterostructures. The oxygen atoms are clearly visible, and the connectivity of oxygen octahedra across the interfaces is indicated. All the LSMO films are 6 uc thick. **e**, Layer-position-dependent mean octahedral tilt angle (β) together with its standard deviation in LSMO/NGO heterostructures with and without a STO buffer layer. The data for the non-buffered sample are shifted upwards by 6° for clarity.

Textured VO2 thin film

VO2 thin film on Al2O3 substrate

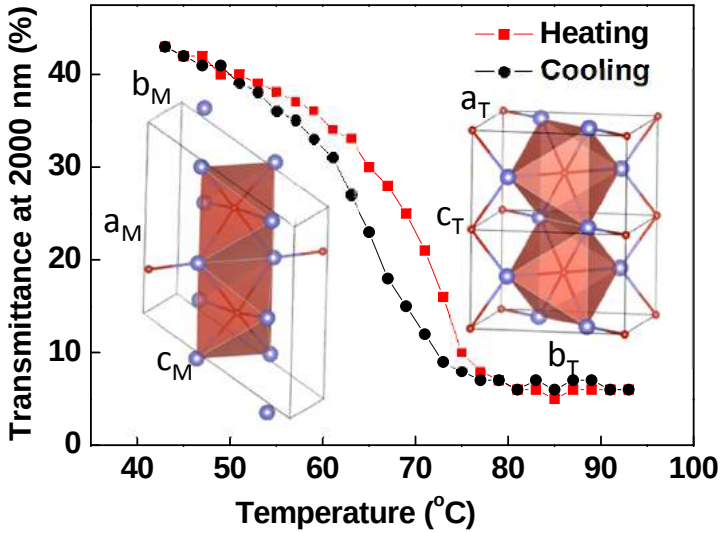

	Space group	a (Å)	b (Å)	c (Å)	α	β	γ
VO_2-M (T<66°C)	$P2_1/c$ (14)	5.75	4.526	5.38	90°	122.6°	90°
VO_2-R (T>66°C)	$P4_2/mnm$ (136)	4.55	4.55	2.88	90°	90°	90°
α-Al_2O_3	R-3c(167)	4.754	4.754	12.99	90°	90°	120°

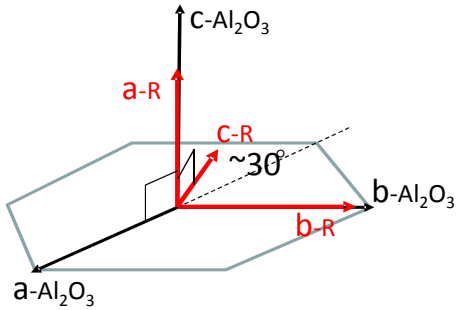

VO2 –R (rutile) on alumina (001 cut)

$a_M=2c_R$
$b_M=a_R$
$c_M=b_R-c_R$

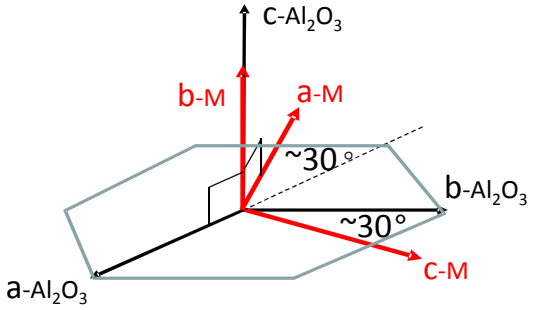

VO2 –M (monoclinic) on alumina (001 cut)

Textured VO2 thin film

Microstructures of the undoped VO_2(M) thin films

Cross-section geometry

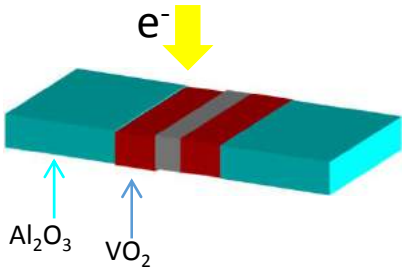

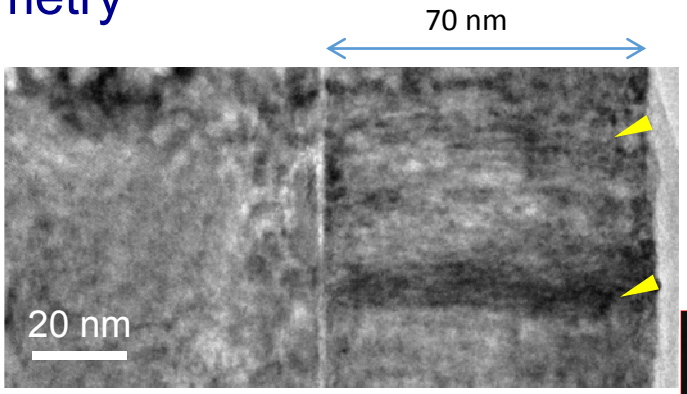

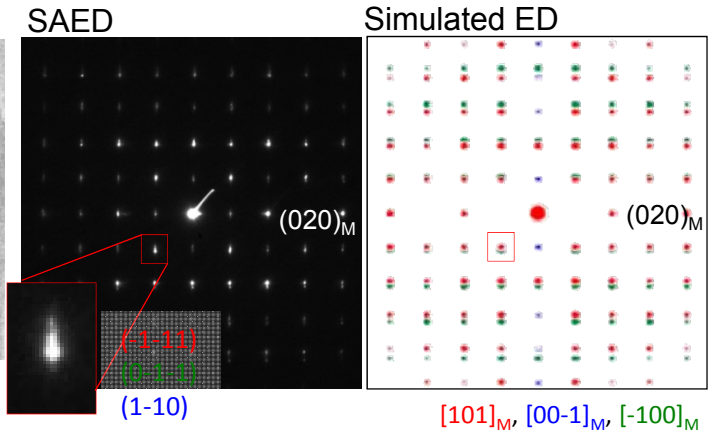

In-plane geometry

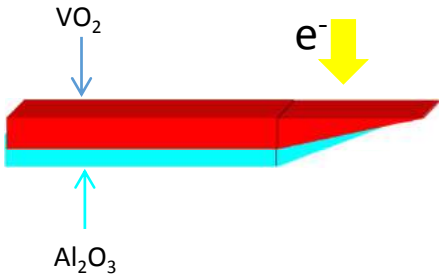

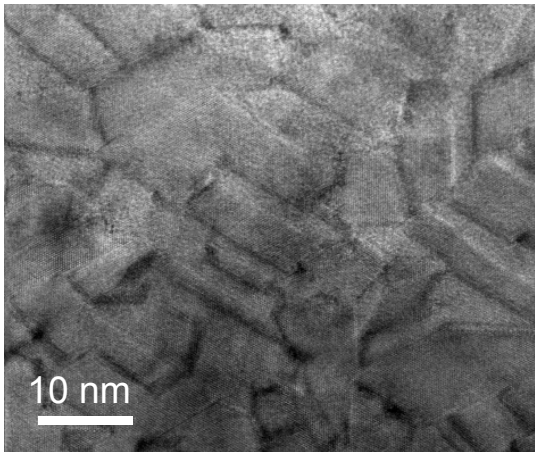

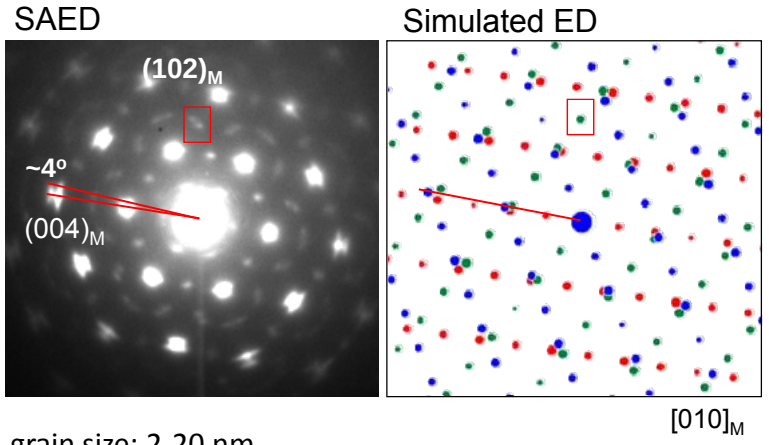

grain size: 2-20 nm

Growth orientation: $VO_2[010]_M//Al_2O_3[001]$ + 3-fold in-plane twinning symmetry+ 2-fold out of plane symmetry + Distorted crystal structure

Textured VO2 thin film

Imaging the grain boundaries and strains

BF (β < 5mrad)

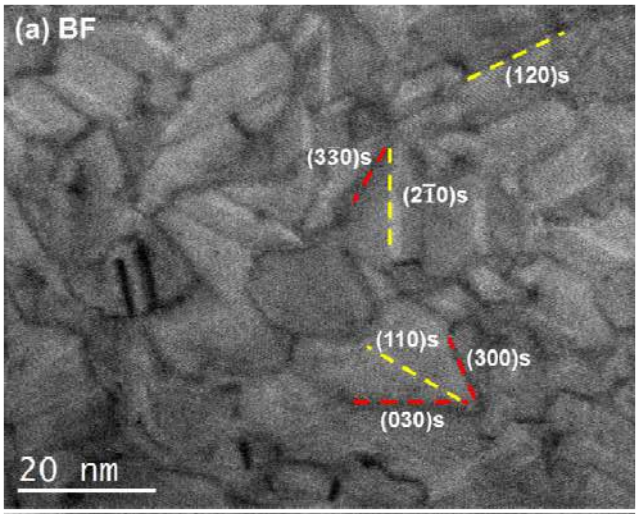

Crystallographic-contrast

HAADF (100 mrad < β < 200mrad)

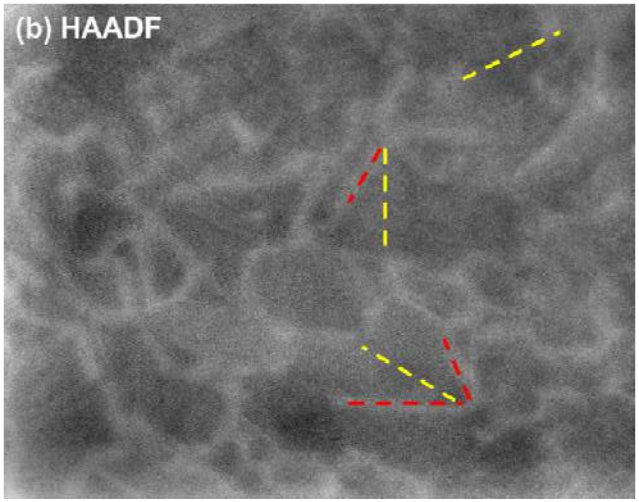

Z-contrast
(mostly)

LAADF (50 mrad < β < 80 mrad)

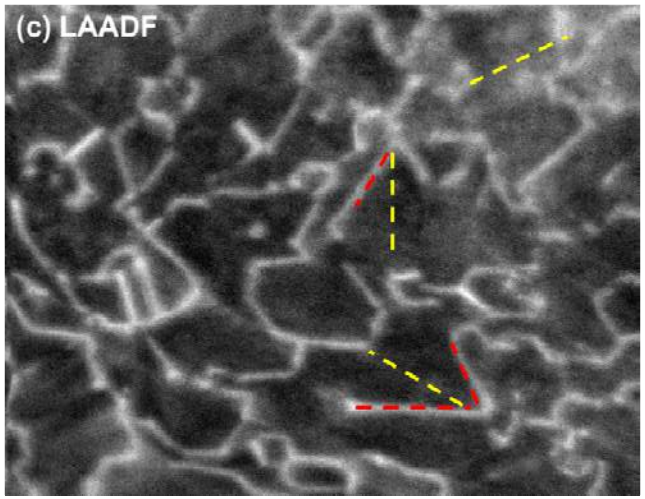

Strain-contrast
disorder, thermal diffuse scattering

- Highly symmetric GB:
  - ONLY **6** different orientations
- Classified into two families:
  - {110}s and {300}s according to the substrate symmetry and contrast
- Enhanced contrasts in STEM-LAADF imaging,

Textured VO2 thin film

Atomic displacements quantification / monoclinic distortion at GBs

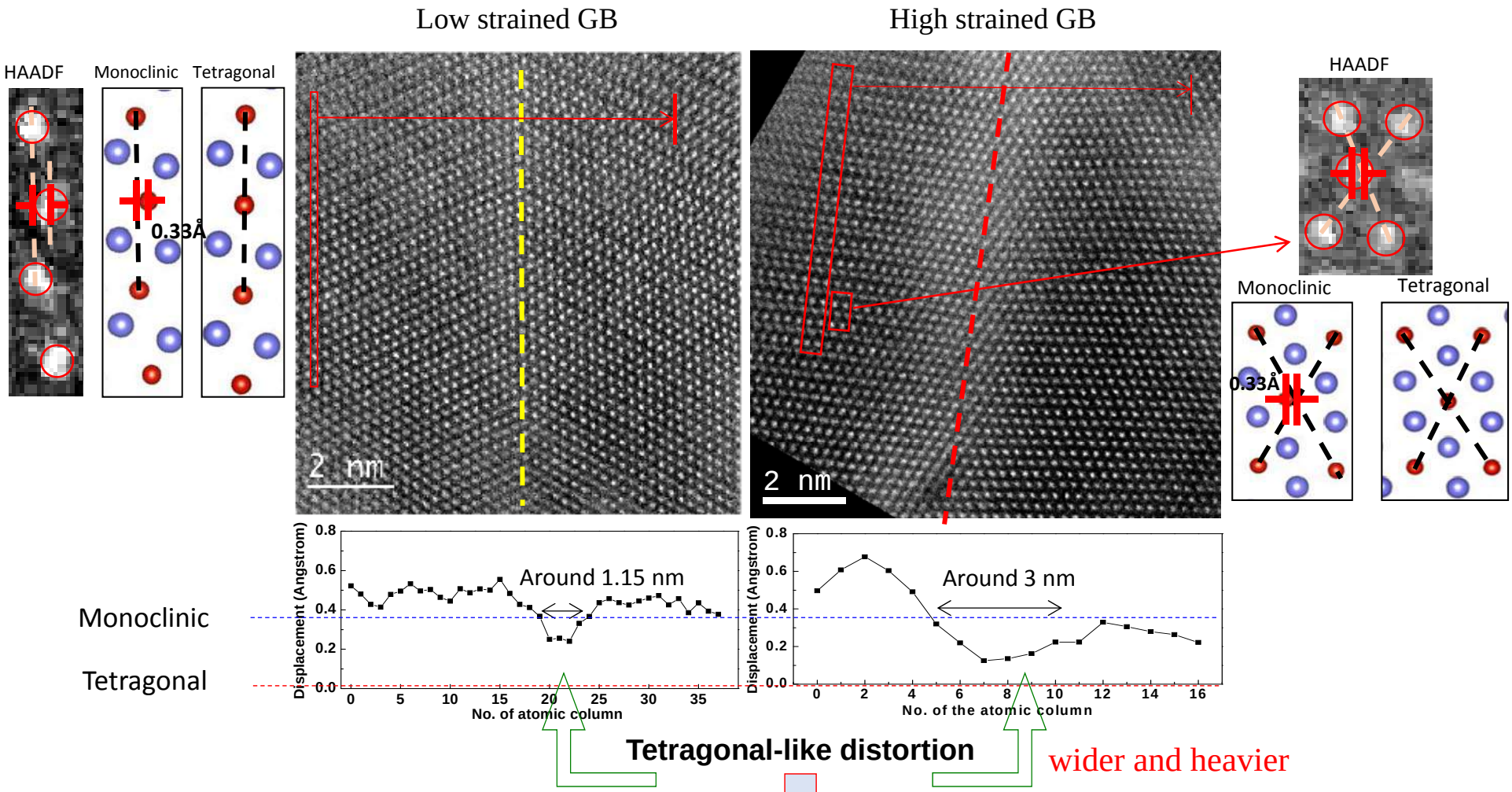

X.Li, et.al, Acta Materialia 61(2013), 6443

Inhomogeneous strain geometry influence the MIT dynamic process

Textured VO2 thin film

Atomic scale observation of defect-mediated first-order phase transition in VO2(A)

Chao Jiang, Lu Chen, Shidong Ji, Jun Liu, Zhengfei Zhang, Ping Jin, Yong Wang, and Ze Zhang

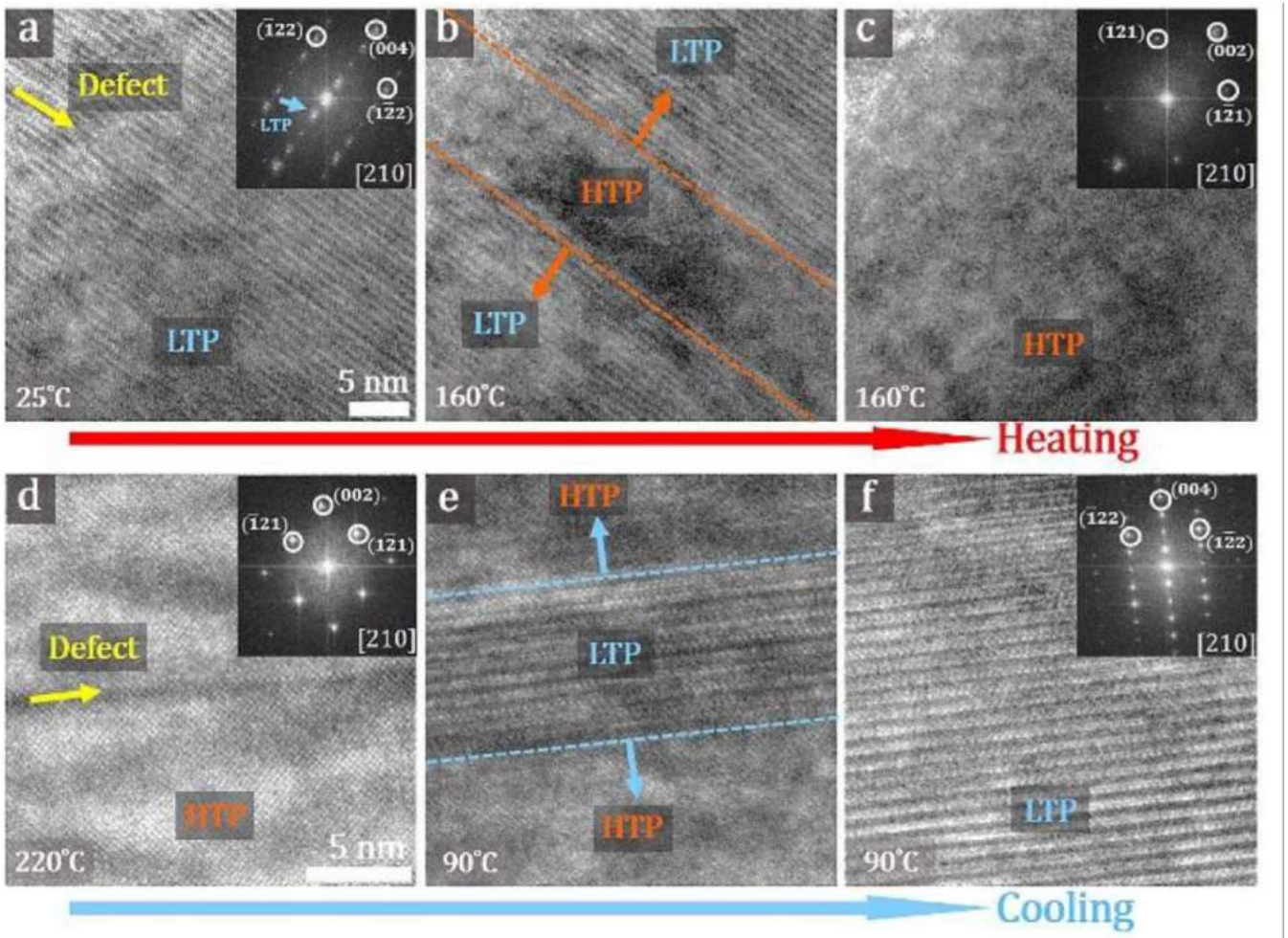

Under press in Nanoscale

In-situ HRTEM images of phase transition originating from defects.
(a-c) *In-situ* HRTEM image series of phase transition from LTP to HTP along [210] zone axis starting at defect in LTP when heating the sample. The defect is highlighted by yellow arrow in (a). The insets are the corresponding fast Fourier transformation (FFT) images. (d-f) *In-situ* HRTEM image series of phase transition from HTP to LTP
along [210] zone axis originating from defect in HTP when the sample was cooled. The defect is highlighted by yellow arrow in (d). The insets are the corresponding FFT images.

Textured VO2 thin film

Atomic scale observation of defect-mediated first-order phase transition in VO2(A)

Chao Jiang, Lu Chen, Shidong Ji, Jun Liu, Zhengfei Zhang, Ping Jin, Yong Wang, and Ze Zhang

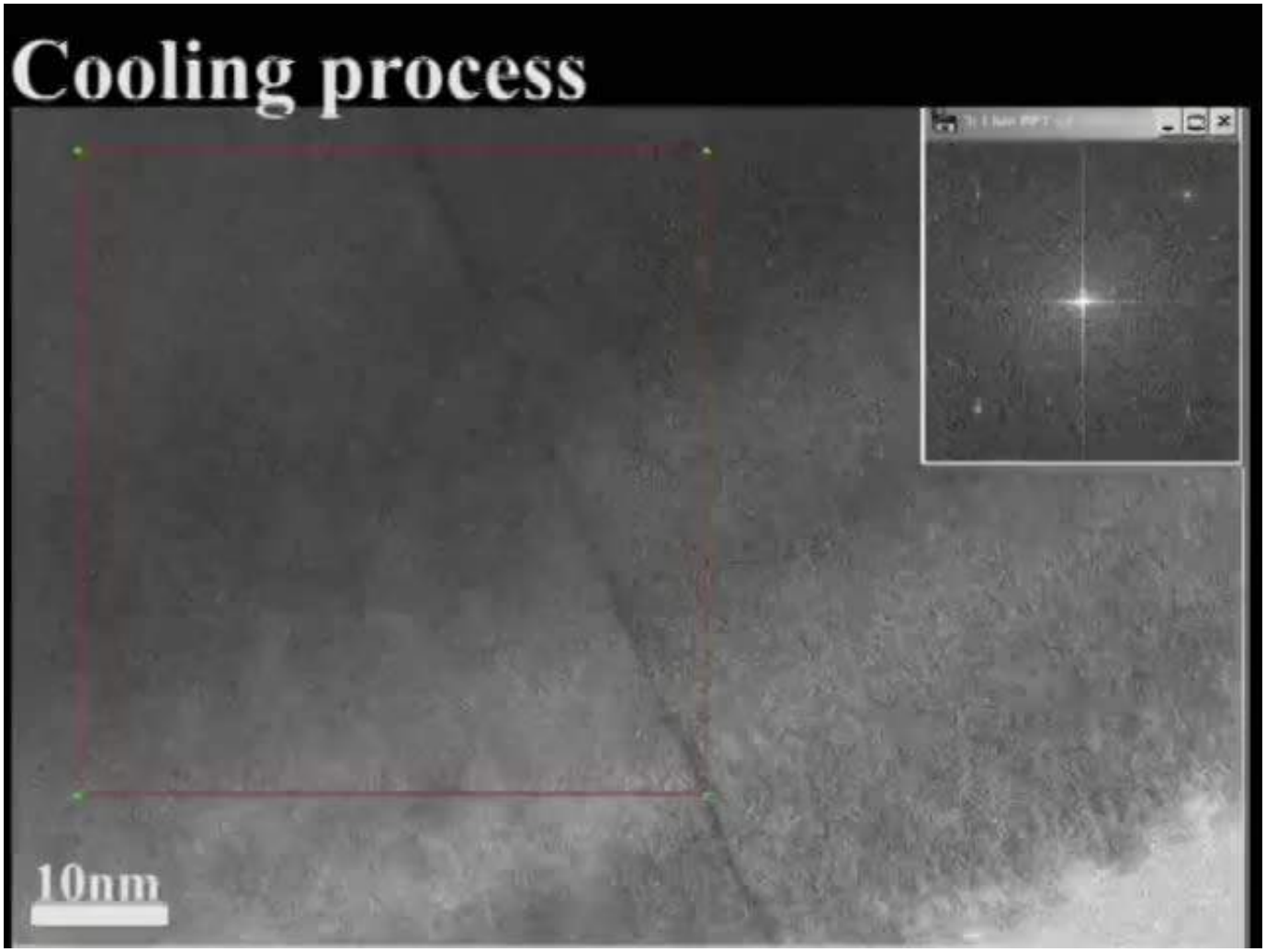

Under press in Nanoscale

Few perspectives

In-situ (temperature, applied voltage) combined with high resolution STEM

Direct observation of oxygen vacancy-driven structural and resistive phase transitions in La2/3Sr1/3MnO3

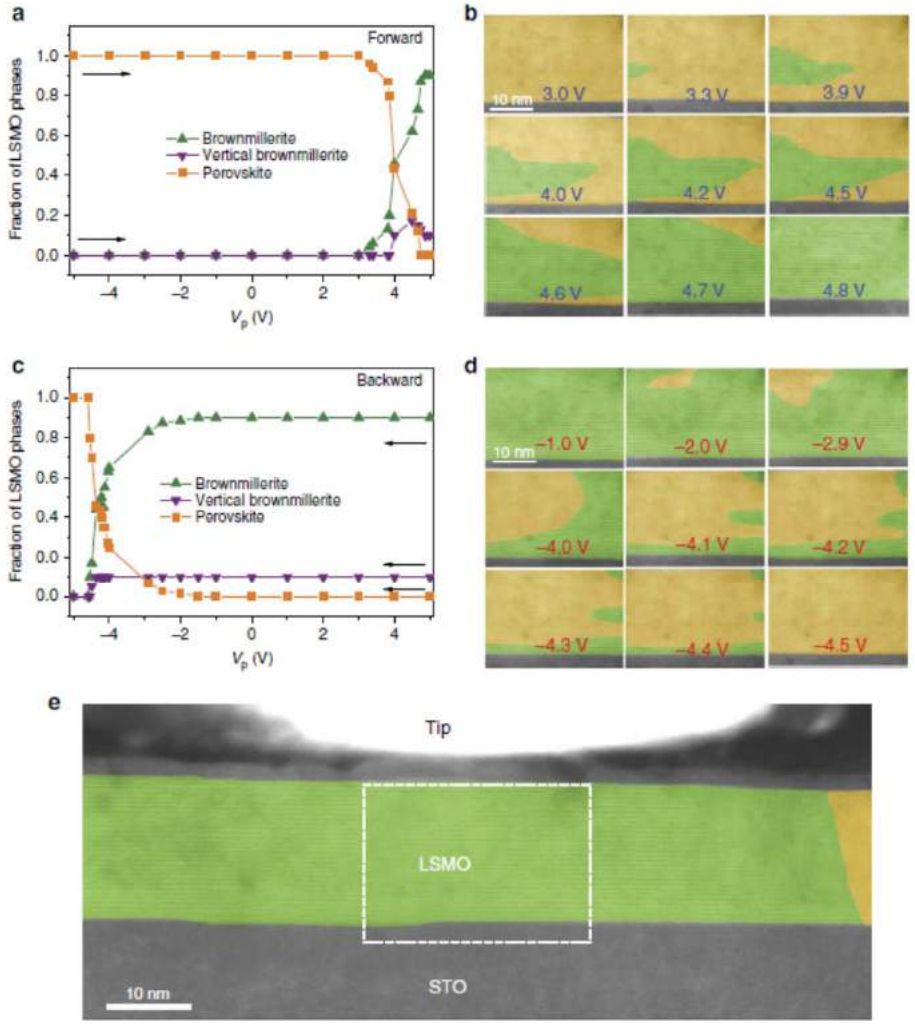

Figure 3 | Evolution of structural phases during resistive switching. (**a**,**c**) Areal fraction of various LSMO phases during the resistive switching experiments of Fig. 1. The forward and backward branches of the switching curves are plotted separately for clarity. Data were collected from a 50 nm-wide LSMO area underneath the metal tip after several switching cycles. (**b**,**d**) STEM images illustrating the growth of brownmillerite (green) and perovskite (yellow) structural phases in the forward (**b**) and backward (**d**) branches of the resistive switching curve. The images have been coloured to more clearly visualize the structural transition. (**e**) Lower resolution STEM image of the saturated high-resistance state. The electrically induced brownmillerite structure (green) forms uniformly over a width of about 100 nm. The dashed line indicates the image area of the results shown in **b**,**d**.

L. Yao et al., Nature Com. 2017

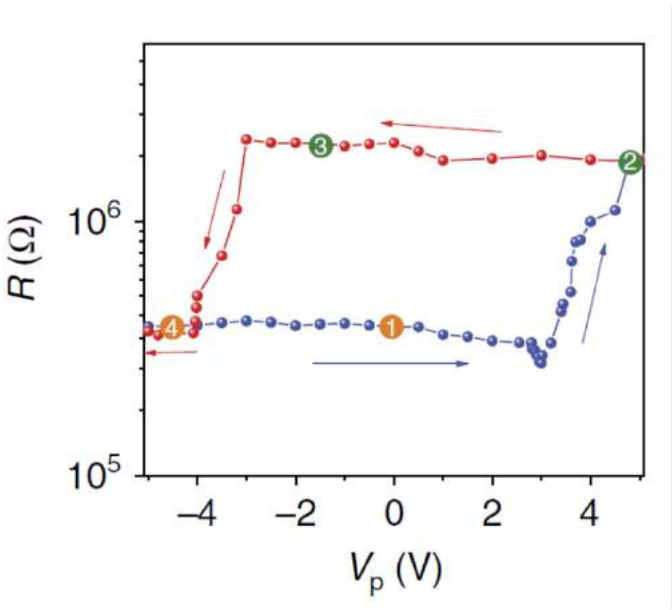

Higher resistivity when Vo get ordered
(Browmillerite ABO2.5 vs Peroskite ABO3)

Few perspectives

Higher spectral resolution STEM-EELS (keeping sub-nanometer spatial resolution)

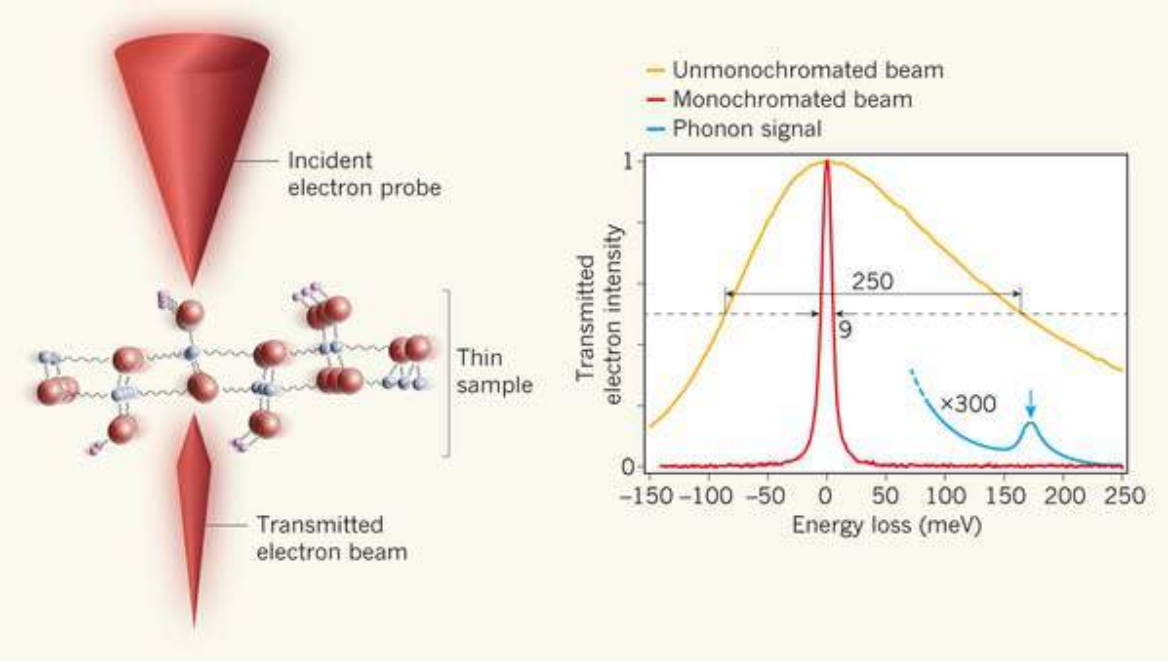

LO phonon in h-BN, with a peak energy of 173meV

Krivanek et al. Nature **514**, 209 (2014).

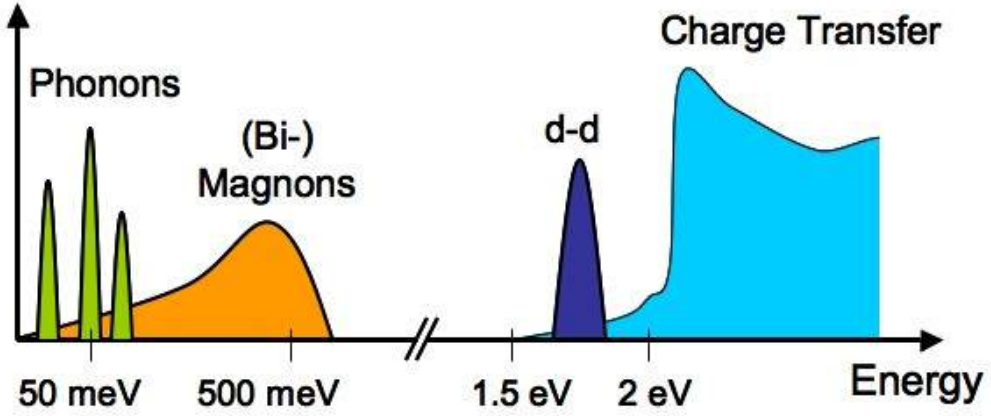

Acknowledgements

STEM group @ LPS-Orsay
https://www.stem.lps.u-psud.fr/

Main collaborators are

- S. catalano, J. Fowlie, A. Torres, D. Li, P. Zubko, M. Gibert, S. Gariglio, J.-M- Triscone, Department of Quantum Matter Physics at the University of Geneva.

- V. Garcia, S. Fusil, M. Bibes, A. Barthélémy, Thales Research and Technology, Campus de l'Ecole Polytechnique, 91767 Palaiseau, France.

- O. Popova, Y. Dumont, N. Keller, Groupe d'ÉtudesdelaMatièreCondensée (GEMaC), Université de Versailles Saint Quentin en Yvelines - CNRS, France

- P. Van Aken, Max Planck Institute for Solid State Research, Stuttgart, Germany

- H. Gu, P. Jin, Shanghai Institute of Ceramics, Chinese Academy of Sciences, China

Few reviews :

C. Colliex et al. Ultramicroscopy 123 p80-89 (2012)
M. Kociak et al. Ultramicroscopy, doi:j.ultramic.2017.02.008 (2017)
A. Gloter et al. Materials Science in Semiconductor Processing, doi:j.mssp.2016.07.006(2016)
I. McLaren and Q. Ramasse, International Materials Reviews 59 pp. 115—131 (2012)
G. Botton et al., Acta Crystallographica Section A 70 1452 (2014)